The Extended Timing Annotation Dataset for Sentinel-1—Product Description and First Evaluation Results

Christoph Gisinger, Ludivine Libert, Petar Marinkovic, Lukas Krieger, Yngvar Larsen, *Member, IEEE*, Antonio Valentino, Helko Breit, Ulrich Balss, Steffen Suchandt, Thomas Nagler, *Member, IEEE*, Michael Eineder, *Fellow, IEEE*, and Nuno Miranda

***Abstract*— This article introduces the extended timing annotation dataset (ETAD) product for Sentinel-1 (S-1) which was developed in a joint effort of German Aerospace Center (DLR) and European Space Agency (ESA). It allows to correct range and azimuth timing of S-1 images for geophysical effects and for inaccuracies in synthetic aperture radar (SAR) image focusing. In combination with the precise orbit solution, these effects determine the absolute geolocation accuracy of S-1 SAR images and the relative collocation accuracy of repeat pass image stacks. ETAD contains the gridded timing corrections for the tropospheric and ionospheric path delays, the tidal-based surface displacements, and the SAR processing effects, all of which are computed for each data taken using standard models from geodesy and auxiliary atmospheric data. The ETAD product helps S-1 users to significantly improve the geolocation accuracy of the S-1 SAR products to better than 0.2 m and offers a potential solution for correcting large-scale interferometric phase variations. The product layout and product generation are described schematically. This article also reports first the results for different SAR techniques: first, the improvement in geolocation accuracy down to a few centimeters by verification of accurately surveyed corner reflector positions in the range–azimuth plane; second, the well-established offset-tracking technique, which is used for systematic ice velocity monitoring of ice sheets and glaciers, where ETAD can reduce velocity biases down to subcentimetric values; and third, the correction of atmospheric phase contributions in wide-area interferograms used for national and European ground motion services. These early results proof the added value of the ETAD corrections and that the product design is well-suited to be integrated into the processing flows of established SAR applications such as absolute ranging of targets, speckle/feature tracking, and interferometry.**

***Index Terms*— Atmospheric phase screen, glaciology, imaging geodesy, InSAR, ionospheric phase screen, natural hazards, radar remote sensing, SAR geodesy, Sentinel-1, speckle tracking, synthetic aperture radar.**

Manuscript received 25 November 2021; revised 23 March 2022 and 20 May 2022; accepted 29 June 2022. Date of publication 27 July 2022; date of current version 17 August 2022. This work was supported by the European Union (EU) Commission's Copernicus Program through the European Space Agency (ESA) under Contract 4000126567/19/I-BG. *(Corresponding author: Christoph Gisinger.)*

Christoph Gisinger, Lukas Krieger, Helko Breit, Ulrich Balss, and Steffen Suchandt are with the Remote Sensing Technology Institute, German Aerospace Center, 82234 Weßling, Germany (e-mail: christoph.gisinger@dlr.de).

Ludivine Libert and Thomas Nagler are with the Environmental Earth Observation Information Technology (ENVEO IT) GmbH, 6020 Innsbruck, Austria.

Petar Marinkovic is with PPO.labs, 2496 The Hague, The Netherlands.

Yngvar Larsen is with NORCE, 9294 Tromsø, Norway.

Antonio Valentino and Nuno Miranda are with the European Space Agency, 00044 Frascati, Italy.

Michael Eineder is with the Remote Sensing Technology Institute, German Aerospace Center, 82234 Weßling, Germany, and also with the Chair of Remote Sensing Technology, Technical University of Munich, 80333 Munich, Germany.

Digital Object Identifier 10.1109/TGRS.2022.3194216

NOMENCLATURE

ALE	Absolute location error.
API	Application Programming Interface.
APS	Atmospheric phase screen.
C3S	Copernicus Climate Change Service.
CR	Corner reflector.
DEM	Digital elevation model.
DLR	German Aerospace Center.
ECMWF	European Centre for Medium-Range Weather Forecasts.
ESA	European Space Agency.
ETAD	Extended timing annotation dataset.
EW	Extended Wide swath.
FM	Frequency modulation.
GNSS	Global navigation satellite system.
IGS	International GNSS Service.
IPP	Ionospheric pierce point.
ITRF	International Terrestrial Reference Frame.
IV	Ice Velocity.
IW	Interferometric Wide swath.
NWM	Numerical weather model.
OT	Offset-tracking.
rms	Root mean square.
S-1	Sentinel-1.
S-1A	Sentinel-1A.
S-1B	Sentinel-1B.
SETAP	Sentinel-1 Extended Timing Annotation Processor.
SAR	Synthetic aperture radar.
SCR	Signal-to-clutter ratio.
SLC	Single-look complex.
SM	Stripmap.
TEC	Total electron content.
TOPS	Terrain Observation with Progressive Scan.
UTC	Coordinated Universal Time.

I. Introduction

SAR sensors have an intrinsically high pixel localization accuracy because the position in an SAR image is governed by the timing of actively transmitted pulses and recorded radar echoes [1], [2]. The SAR range distance is inferred from the echo runtime which can be determined readily with a precision corresponding to centimeters or even millimeters, depending on the quality of the oscillator [3], [4]. Azimuth localization is determined by the synthetic aperture, i.e., the flight track and the referencing of the SAR clock to the orbit time. It could be determined down to millimeters but is currently often limited to decimeters due to the lack of precision in absolute time referencing. When converting these highly precise range and azimuth time measurements into space coordinates, the wave propagation through the neutral troposphere and the dispersive ionosphere, and the uncertainty on the orbit position are the dominating error sources.

As known from comparisons with tropospheric path delays observed with global navigation satellite system (GNSS) technology, the propagation delay can be computed with an accuracy of a few centimeters by integration of numerical weather models [5]–[8], and the ionospheric state can be defined by physical models or inferred from observations of global GNSS networks [9]–[11], allowing for the correction of ionospheric path delays in single-frequency microwave data. As for the orbit position, even 25 years ago satellite orbit state vectors could be determined with 7 cm radial root mean square (rms) and 30 cm along-track rms [12] and can be determined with 2–3-cm position accuracy today [13]–[16]. However, the geometric accuracy of SAR systems was not fully exploited so far. This might be due to the lack of requirements on the geometric SAR products and the consequent lack of thorough analysis and algorithm design, which were in contrast developed by the GNSS community, see, for instance, Teunissen and Montenbruck, 2017 [17]. For the sake of conciseness, we list here only the main contributions and error sources that are neglected in most of the currently available operational SAR products: atmospheric propagation delay through troposphere and ionosphere (2-4 m); inaccurate azimuth time referencing between SAR and GNSS clock (0.2 m); SAR focusing inaccuracies such as stop-go-approximation (<3 m); implications of GNSS-based orbit determination; and the geodynamic deformations associated with the underlying geodetic reference frames (<0.2 m). A more detailed explanation can be found in [18]–[21], where it is shown that a breakthrough in geometric accuracy can only be achieved if all the aforementioned affects are considered properly.

In consequence, ESA and DLR investigated the technical capabilities of S-1 mission and the design of an S-1-based SAR product with geodetic accuracy. The results are the calibration procedures described in [22] and the very promising results published in [23]. Based on this initial analysis, the ETAD product was designed. The goal of ETAD is to provide a wide range of users with a product easy to use, so they can benefit from the geodetic accuracy of SAR without dealing with the details of the SAR processing technology and the standards and techniques used in geodesy. The product is designed as a correction layer to be applied by the user, which avoids the modification of the original SAR data distributed by ESA and leaves the possibility to consistently apply the corrections to datasets derived from the original SAR scenes as delivered by ESA. The algorithms have been implemented into an operational software for the S-1 ground segment that can be potentially used to generate correction data for every scene acquired by the S-1A/B fleet.

In subsequent pilot studies, the ETAD product has been tested and validated for two S-1-based products of operational services: the monitoring of the Greenland ice sheet flow velocity applying SAR offset-tracking (OT) and ground motion monitoring in Norway with SAR interferometry. OT is a technique that aims at estimating the local shifts between two SAR images, which are mostly related to ice motion when observing glaciers and ice caps [24]–[27]. However, these offsets are impacted by uncorrected timing delays, especially for ice caps at high latitudes where the ionosphere can introduce severe shifts in the SAR data. ETAD constitutes a promising solution for correcting timing-related biases in S-1 OT measurements, and its use is investigated in the case of ice velocity monitoring over the Greenland ice sheet.

The second application is ground motion mapping using SAR interferometry. Spatially correlated atmospheric phase screens are the most dominant error source in interferometry. Extensive workshops and studies have been performed by UNAVCO/United States (US) [28] and ESA [29], trying to reduce the atmospheric phase screen with numerical weather models (NWMs) and data-driven methods. The general conclusion was that NWMs does currently not provide the resolution and accuracy to reliably correct high-resolution SAR interferograms. The 10-km horizontal resolution of the operational integrated forecast system (IFS) analysis data from the European Centre for Medium-Range Weather Forecasts (ECMWF) [30], which we use as background data, is indeed insufficient for high-resolution phase correction. Instead, our ETAD product targets on tropospheric phase errors with correlation lengths larger than 50 km and on systematic errors caused by changing atmospheric refraction in areas with significant topography. We tested this ability on large-area interferograms in Norway which are used for the national ground motion service and the upcoming European Ground Motion Service (EGMS). Even if the ETAD product was primarily defined for centimetric range/azimuth corrections, the range component can be used to model tropospheric delay variations and reduce stratified phase errors in interferograms with convincing results.

This article is structured as follows: Chapter II introduces the architecture of the ETAD product and the algorithms to generate it. The validation of ETAD applying SAR geolocation was carried out by DLR and is reported in section III. In section IV and V, we report on the first demonstration and the independent assessment of ETAD in ice velocity monitoring and SAR interferometry performed by Environmental Earth Observation Information Technology GmbH (ENVEO) and PPO.labs, respectively, which were not involved in the product development. Finally, section VI summarizes the key

TABLE I
ACCURACY SPECIFICATION OF ETAD CORRECTIONS AND NOMINAL LOCATION ACCURACY SPECIFICATION OF S-1 SLC PRODUCTS [31], [33]

SAR mode	ETAD products (1 sigma)		S-1 SLC products (3 sigma)	
	Rg [m]	Az [m]	Rg [m]	Az [m]
TOPS IW	0.2	0.1	7.0	7.0
Stripmap	0.2	0.1	2.5	2.5

aspects and provides an outlook on the operational generation of ETAD products by ESA.

II. ETAD PRODUCT

A. Features and Contents

The S-1 single-look complex (SLC) image products are processed for the zero-Doppler geometry convention [31]. Consequently, the 2-D coordinates annotated to the SAR images, slant range time τ and azimuth time t, describe an orthogonal raster for which every range line of positions on the ground $\mathbf{X}$ corresponds to a single azimuth time t linked to the sensor's state vector $\mathbf{X}_s(t), \dot{\mathbf{X}}_s(t)$. This is summarized by the SAR range Doppler equations in zero-Doppler configuration [2], [32]

$$\tau = 2/c \cdot |\mathbf{X}_s(t) - \mathbf{X}| \tag{1}$$

$$0 = \frac{\dot{\mathbf{X}}_s(t)(\mathbf{X}_s(t) - \mathbf{X})}{|\dot{\mathbf{X}}_s(t)||\mathbf{X}_s(t) - \mathbf{X}|} \tag{2}$$

where c denotes the speed of light in vacuum. The fulfillment of these equations by an SLC image product with respect to the true positions on the ground defines the geolocation quality and thus the geometric fidelity of the SAR system. For the S-1 products demanding near real-time processing and distribution, the nominal specification of absolute geolocation accuracy is listed in Table I, which does not involve any additional timing corrections for path delays or surface deformation. Improving the meter-level geolocation accuracy to well below the submeter level and maximizing the geometric fidelity of operational S-1 products are the main goals of the ETAD product and its timing corrections. The overall accuracy of ETAD corrections (1 sigma) at a global level is specified with 0.2 m range and 0.1 m azimuth; see Table I. These numbers are based on the accuracy of the used correction methods and the underlying input data; see section II-B. It is important to note that the absolute geolocation accuracy evaluates the entire SAR system, involving effects not controlled by the ETAD product, e.g., SAR antenna phase center offset, finite azimuth time quantization or oscillator aging. Therefore, formal ETAD specifications apply only to the standalone product and do not specify an attainable geolocation accuracy of S-1 SLC products. However, the validation results documented in this publication show that in practice the S-1 SAR system can even exceed these specifications when applying ETAD corrections.

The ETAD product is directly computed from the annotations of S-1 level 1 SLC products and auxiliary data comprising the precise orbit files, atmospheric model data, and the solid Earth tide model, which are described in Section II-B. This allows the generation of extended timing corrections for every S-1 SLC acquisition in the catalog. At the time of writing, the product has a latency of 21 days after an acquisition because of the usage of the S-1 precise orbit solution. Currently, the ETAD product is qualified for the two S-1 modes Interferometric Wide swath (IW) and Stripmap (SM) [31], but the processing of Extended Wide swath (EW) mode is already possible at an experimental level. The detailed ETAD format specification is available from ESA [34].

The ETAD product contains slant range and azimuth timing corrections for tropospheric delays, ionospheric delays, solid Earth tides, the S-1 system effects stemming from SAR processing, and instrument calibration constants. It is delivered in the Standard Archive Format for Europe (SAFE) structure [35]. The product contains the extracted precise orbit segment specific to the data take, a quicklook file, and the two core ETAD components: the ETAD Network Common Data Form (NetCDF) product and the ETAD Extensible Markup Language (XML) product. The ETAD XML product provides fast access to grid definitions of the individual bursts and contains statistics for timing corrections of each burst. In addition, it contains auxiliary information about processing parameters and lists the used input data products.

The NetCDF product provides correction data grids. It is a self-contained file that has all necessary information for the application of corrections of SLC SAR timings or the generation of InSAR phase screens. It defines a grid equally spaced in time which encompasses the entire S-1 data take and which is annotated by fast time τ (range) and slow time t (azimuth). Depending on the SAR mode of the corresponding S-1 SLC product, the NetCDF contains a number of groups equal to the number of swathes acquired in this mode. These swath groups contain subgroups for each burst. Consequently, the internal structure is closely following the underlying SAR SLC data [31]; see Fig. 1. For SM acquisitions, an entire SM slice is treated as a single burst. The reason for this burst-wise handling of corrections are the S-1 system corrections which differ in overlapping bursts and swaths.

The NetCDF burst groups contain individual corrections in seven NetCDF layers as shown in Fig. 3, plus two additional layers for the sum of range and sum of azimuth corrections. The range and azimuth times of the correction grid nodes are annotated in two vectors. Moreover, three layers define the corresponding latitude, longitude, and height coordinates of the grid points. It has to be noted that the sum layers already contain the timing calibration constants for the sensor. All the timing corrections are given in units of seconds. Additional information, e.g., for selecting a subset of corrections or to transform the timing corrections into metric shifts, are annotated as attributes of the respective NetCDF groups [34].

The achievable accuracy when applying the ETAD timing corrections is driven by the entire S-1 system, which also involves any bias stemming from internal electronic delays, polarization-dependent biases, orbit errors, or potential biases of the applied geophysical corrections. Consequently, the ETAD product generation uses a sensor calibration for range and azimuth timings, which accounts for the overall system biases and which has to be determined empirically. The initial

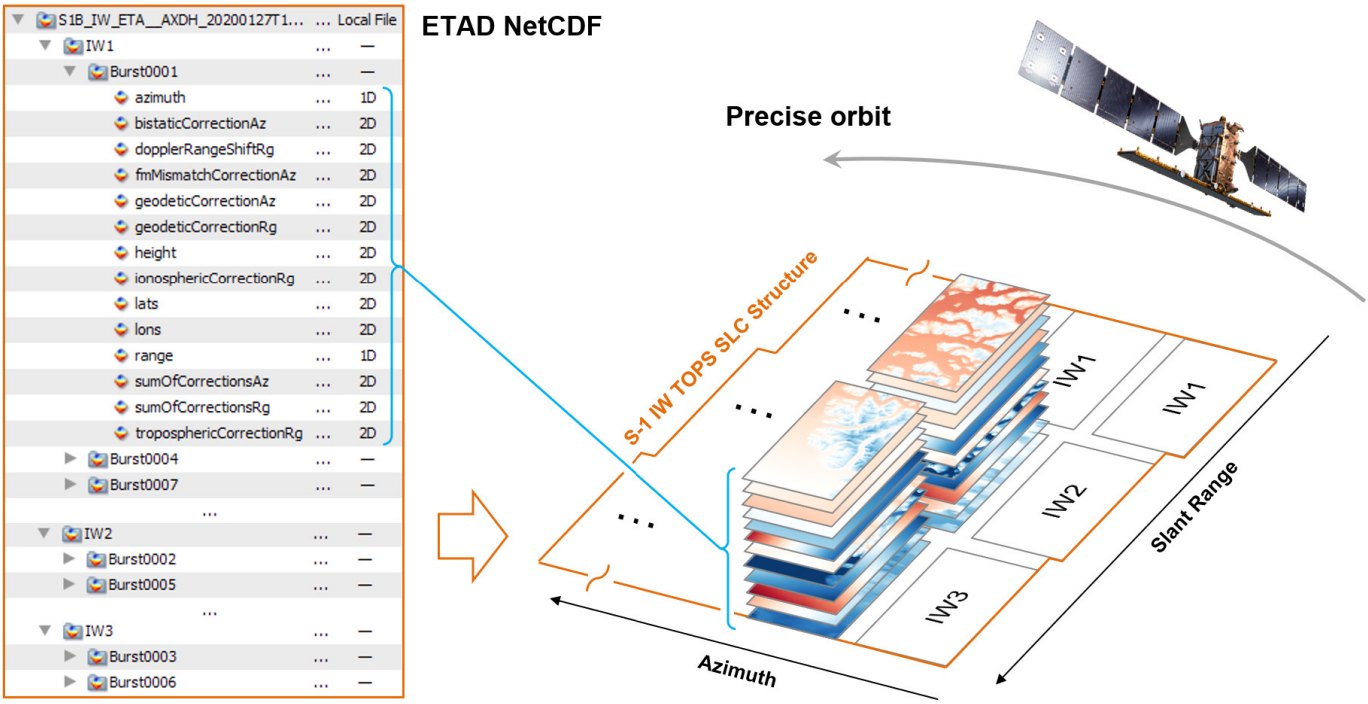

Fig. 1. ETAD NetCDF product is structured hierarchically in groups for each subswath and burst which contain a stack of nine correction grids and three coordinate grids. The individual burst correction grids lie on a continuous range and azimuth time grid encompassing the whole data take. The range and azimuth times defining the grid of a given burst are annotated as 1D vectors.

TABLE II
INITIAL SENTINEL-1 TIMING CALIBRATION CONSTANTS FOR S-1 ETAD PRODUCT AND CORRESPONDING NUMBERS IN UNITS OF METERS

Sensor	$\Delta\tau_{cal}$ [s]	Δt_{cal} [s]	Rg [m]	Az [m]
S1A	$1.1281e^{-9}$	$1.2873e^{-5}$	0.1691	0.0875
S1B	$0.0646e^{-9}$	$-4.9701e^{-5}$	0.0097	−0.3380

values of the used auxiliary file stem from a calibration that DLR performed at the Metsähovi calibration site, Finland, with three years of S-1A and S-1B IW data (2017–2020) and corrections according to the ETAD methods. The Metsähovi station contains a very stable corner reflector (CR) with 1.5 - m edge length, which was also used for accurate geometric recalibration of the TerraSAR-X mission [21]. For details on accurate geometric SAR calibration, see [22], [23]. The initial calibration contains numbers for range and azimuth and S-1A and S-1B, respectively, which are used for all SAR modes, beams, and polarizations; see Table II. Maintenance will be carried out by the S-1 Mission Performance Cluster that regularly performs sensor and product evaluations [36]. The applied timing calibration values are also annotated in the ETAD product NetCDF and are completely transparent to the user.

B. Algorithms and Processing Chain

The Sentinel-1 Extended Timing Annotation Processor (SETAP) software was implemented according to S-1 ground segment requirements to generate ETAD products on an operational basis. The computations are based on the sliced S-1 level 1 SLC products forming a data take [31]. They are provided to the processor along with the S-1 precise orbit ephemeris product; see the schematic workflow shown in Fig. 2. For performance optimization, steps that refer to data take slices and bursts are run concurrently. A crucial step is to define a correction grid that consistently covers all the provided input data. The grid is calculated in range and azimuth as two-way times and as delta times in seconds with respect to a minimum ETAD product Coordinated Universal Time (UTC) time, respectively. The spacing is predefined and corresponds on average to a 200- m ground sampling in both the dimensions. The grid of radar timings is geolocated on a digital elevation model (DEM), i.e., the Copernicus 90-m DEM, [37], to define the 3-D sensor-to-ground geometry, and the geoid model EGM2008 (Earth Gravitational Model 2008, [38]) is imported as well at this point for converting the mean sea level referenced DEM heights into ellipsoidal heights (World Geodetic System (WGS)-84, [39]). With the satellite positions and the 3-D coordinates of the computational grid known, the ETAD corrections are computed with the methods described below, for which additional details can be found in our earlier publications [7], [21], [23] and in the processor algorithm technical baseline document [40]. Note that the corrections for tropospheric and ionospheric delays, solid Earth tides, and the bistatic azimuth correction are computed for all S-1 input products, whereas corrections for Doppler shifts in range and FM rate mismatch shifts in azimuth only apply to the TOPS mode data [23]. The results of different corrections are shown in Fig. 3 for an S-1 data take acquired over Alaska, USA.

1) Direct Integration of NWM for Tropospheric Delays: The tropospheric delay is retrieved by numerical integration

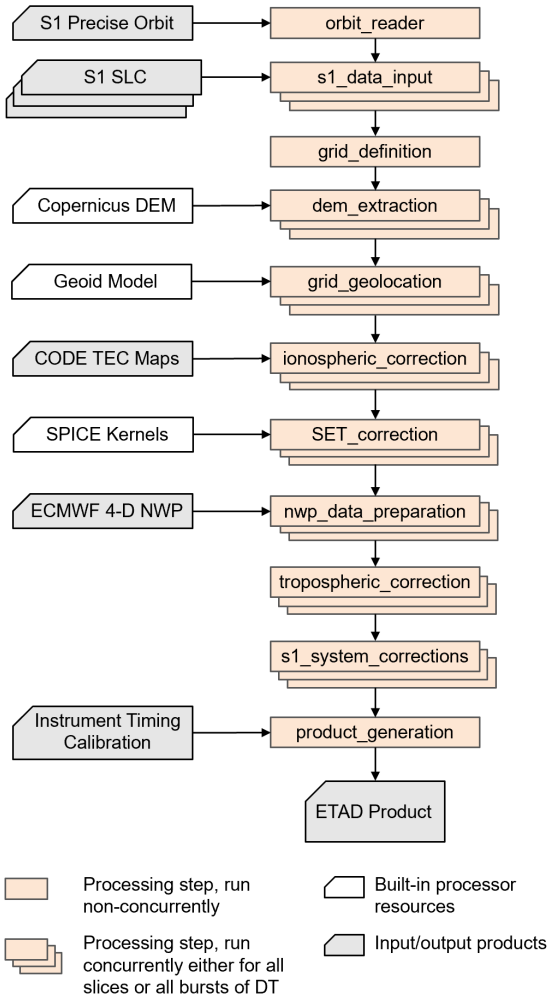

Fig. 2. SETAP processing chain with the steps for correction calculation and for preparation of the input data. For performance optimization, several parts of the processor are run concurrently on the S1 input data take slices or bursts.

of air refractivity modeled along the geometrical line-of-sight between the sensor and the grid point on ground. For the steep to medium incidence angles of S-1 acquisitions (20° - 45°), there is no need to consider the additional ray bending effect because its contribution reaches only a few millimeters at the most [41]. The total tropospheric delay is on the order of 2 to 4 m, depending on the terrain height and local incidence angle. The air refractivity can be expressed as a function of temperature T, pressure P, and specific humidity q. All the three parameters are available in the analysis data of the operational IFS model of ECMWF in 6-h time intervals (00 h, 06 h, 12 h, 18 h UTC) in 3-D, i.e., as a number of 137 vertically stacked 2-D layers (model levels) with a horizontal spatial resolution of approximately 10 km [30], [42]. The direct integration is carried out over discrete intervals ΔR in line-of-sight direction and between z_g and $z_{ML,\text{top}}$, the mean sea level heights of the grid point and of the top model layer, respectively, requiring the involved NWM data to be properly interpolated horizontally and vertically for each integration step n

$$\text{SPD}_{\text{tro}} = 10^{-6} \sum_n \left(k_1 \frac{P_n}{T_n} + k_2' \frac{e_n}{T_n} + k_3 \frac{e_n}{T_n^2} \right) \Delta R \quad \text{for} \quad n \mid z_g \le z_n \le z_{ML,\text{top}} \tag{3}$$

with $e_n \cong q_n P_n/\varepsilon$, $\varepsilon = R_d/R_w$, $R_d = 287.0$ JK^{-1}kg^{-1}, $R_w = 461.51$ JK^{-1}kg^{-1} (gas constants for 1 kg of dry air and water vapor, respectively, [43]), $k_2' = (k_2 - \varepsilon k_1)$, $k_1 = 0.776$ KPa^{-1}, $k_2 = 0.715$ KPa^{-1}, and $k_3 = 3750$ K^{2}Pa^{-1} [7], [44]. The integration is performed for NWM time instants that most closely precede and succeed the grid point's azimuth time. The two slant path delay results are then linearly interpolated for the given grid time t_g, and the outcome is converted into a two-way slant range delay using the speed of light in vacuum

$$\Delta\tau_{\text{tro}} = \text{SPD}_{\text{tro},\,t_g} \cdot 2/c. \tag{4}$$

In an earlier study, we validated the ECMWF-based path delays computed with the described method against GNSS-based path delays observed with the global GNSS network [7], which agree within 1-2 cm for most mid- to high-latitude stations and within 2–4 cm for stations in the equatorial region. These findings are in line with other published results on tropospheric path delays derived from ECMWF data [5], [6], [8].

2) Ionospheric Delay Computation From GNSS-Based TEC Maps: Free electrons and charged particles in the ionosphere cause frequency-dependent path delays for microwave signals. Global ionospheric maps derived from GNSS observations of the global International GNSS Service (IGS) network define the state of the ionosphere by the vertical total electron content (TEC) condensed to a single spherical layer [9], [45]. The SETAP uses as input the daily sets of TEC maps $E_{\text{vTEC}}(\Phi, \lambda)$, horizontally referenced to geocentric latitude Φ and longitude λ with a resolution of 2.5 by 5°, which are provided by the Center of Orbit Determination in Europe (CODE) in the framework of IGS [46]. The TEC can be readily scaled to frequency-dependent delays of the S-1 C-band by applying (5). For a given correction grid point, the vTEC is interpolated at the location of the ionospheric pierce point (IPP), defined as the line-of-sight intersection with the spherical model layer. The temporal vTEC interpolation for the grid point's azimuth times t_g considers the time difference in the grid with respect to the two used TEC maps (before and after data acquisition). The result is the ionospheric delay in slant range in units of seconds, which is obtained as

$$\Delta\tau_{\text{ion}} = \frac{2 \cdot C_I}{c \cdot f_{S1}^2 \cdot \cos(z')} \cdot E_{\text{vTEC}}\left(\Phi_{\text{IPP}}, \lambda_{\text{IPP}}, t_g\right) \cdot \alpha \tag{5}$$

where C_I is the TEC proportionality factor $40.3 \cdot 10^{16}$ m^{3}s^{-2} [47], E_{vTEC} is the vertical TEC model interpolated in space and time, c is the speed of light in vacuum, f_{s1} is the S-1 radar frequency in hertz, and $\cos(z')$ is the ionospheric mapping function depending on the IPP zenith angle. The ionospheric delay may reach up to 1 m for the S-1 C-band.

Moreover, the algorithm has to account for the fact that the S-1 orbit, having an altitude of around 712 km, is still within the upper region of the ionosphere. The equation therefore contains an additional parameter $\alpha = 0.9$ to reduce the

GNSS-based vTEC that comprises the entire ionosphere. The empirical value is based on an earlier analysis performed with TerraSAR-X [21] and was adjusted for S-1. This constant scaling parameter can only approximate the fraction of the electron concentration applicable for S-1 data, but the impact is considered small and the applied scaling remains transparent to users as the parameter is also given in the ETAD product annotation.

The accuracy of the computed ionospheric delays reflects the station distribution and resolution of the IGS GNSS network providing the TEC data. The estimated spatial quality is published along with each solution, and qualitative assessments show an accuracy of 4-5 total electron content unit (TECU) over open ocean and 1-2 TECU over most land areas [9]. This corresponds to 7–8 cm and 2–3 cm, respectively, in slant range C-band SAR data.

3) Solid Earth Tidal Displacement Computation: Solid Earth tides are deformations of the Earth crust caused by the gravitational force of the Sun and the Moon. The signal typically varies between ±25 cm in the vertical direction, but there is also a significant horizontal displacement of up to 6 cm [48]. At a global scale, which is the focus of the ETAD product, the direct tides are the dominating solid Earth displacement signal, but one should be aware that there are also ocean tide loading effects that can reach several centimeters at certain coastal regions [48].

The tides' computation requires the time-dependent constellation of the Sun and the Moon as seen from the Earth, as well as a geodynamic model describing the deformation ability of the solid Earth. The model applied in ETAD is the conventional model of the International Terrestrial Reference Frame (ITRF) which is described in detail by the conventions associated with geodetic reference frames [48]. For the position vectors of the Sun and Moon, the conventions refer to the D421 planetary ephemerides issued by National Aeronautics and Space Administration (NASA) Jet Propulsion Laboratory (JPL). These are retrieved using NASA's SPICE toolkit Application Programming Interface (API) [49]. The 3-D tidal displacement vector is obtained in units of meters in the global ITRF. Thus, the result requires a conversion into slant range and azimuth timing geometry of the correction grid. This is done by computing the zero-Doppler radar times of the grid position including the tidal displacement and calculating the difference to the grid nominal radar times. Single Sentinel-1 SAR acquisitions can span several thousands of kilometers in the North–South direction; see Fig. 3, for which the tidal effect within one data take may vary up to 20 cm in slant range (peak-to-peak). For repeated acquisitions, the SAR data time series will eventually observe shifts of the Earth surface that have up to 25 cm amplitude.

The tide model considers all the signal components with contributions larger than 1 mm and can be considered inherently accurate because it is firmly embedded in the crust-based ITRF [48]. The frame conventions are also applied for the generation of the S-1 precise orbit solution [13]. Therefore, we remove the high-frequency time variations in the solid Earth tides but we do not apply any additional correction for secular surface deformations such as tectonics. This means that users will be able to observe signals of tectonic deformations and comparison with reference targets require proper consideration of the ITRF epoch [23].

4) Bistatic Azimuth Effects Mitigation: The motion of the S-1 satellites between pulse transmission and echo reception amounts to approximately 30–40 m. This quasi-bistatic situation is commonly neglected as SAR focusing schemes apply the stop-and-go approximation: it is assumed that the satellite stops between transmission and reception of a single pulse and only moves after each cycle [1]. This is beneficial with respect to computational efficiency, but the implications have to be carefully considered to generate SAR images of rigorous zero-Doppler geometry, i.e., with orthogonal t and τ (azimuth and range) annotation. The S-1 SAR processor applies a simple shift to modify the azimuth timing annotation [31], thereby leaving subpixel distortions and range dependent shifts of 2-4 m in the azimuth times of the S-1 products. The algorithm for the postprocessing correction Δt_{BA} therefore determines both the inverse of the original azimuth shift and the rigorous correction for each correction grid point as [23]

$$\Delta t_{BA} = \frac{\tau_{\text{mid}}}{2} + \frac{\tau_g}{2} - \text{rank} \cdot \text{PRI} \tag{6}$$

with τ_{mid}, τ_g, and pulse repetition interval (PRI) being the reconstructed mid-swath range time, the range time of the correction grid point, and the pulse repetition interval of the considered burst, respectively. The parameter rank specifies the number of PRI events between transmitted pulse and return echo. All the required parameters are annotated in the S-1 SLC SAR product [50]. Because rank and PRI change from subswath to subswath, the correction changes considerably across the swath, especially so with IW3; see Fig. 3.

5) Doppler-Induced Range Shift Mitigation: The transmitted radar pulses experience frequency shifts from the Doppler effect caused by the satellite's motion. These shifts are usually ignored by SAR image processing, because the effect cancels almost completely for SAR modes with azimuth spectra close to zero-Doppler, e.g., stripmap SAR with zero-Doppler steering. However, for the Terrain Observation with Progressive Scan (TOPS) mode used by S-1, which generates data with large Doppler centroid variations across the bursts, the impact of the Doppler shift becomes significant, especially toward the edge of the bursts where the Doppler effect is the largest [23]. During spectral range compression, the Doppler frequency leads to a proportional spatial shift of the compressed pulses. This is not handled by the S-1 SAR processor for the IW and EW data and the shifts ranging between ±0.4 m across each burst have to be removed; see Fig. 3. The correction value

$$\Delta\tau_{\text{DRS}} = f_{dc,g}/K_r \tag{7}$$

is proportional to the Doppler centroid frequency $f_{dc,g}$ for the grid point location t_g, τ_g which has to consider the beam steering of the TOPS mode [23]. K_r denotes the frequency modulation (FM) rate of the range chirp annotated in the SAR products [50].

6) FM Rate Mismatch Azimuth Shift Mitigation: Focusing of the azimuth signal requires knowledge of the azimuth FM

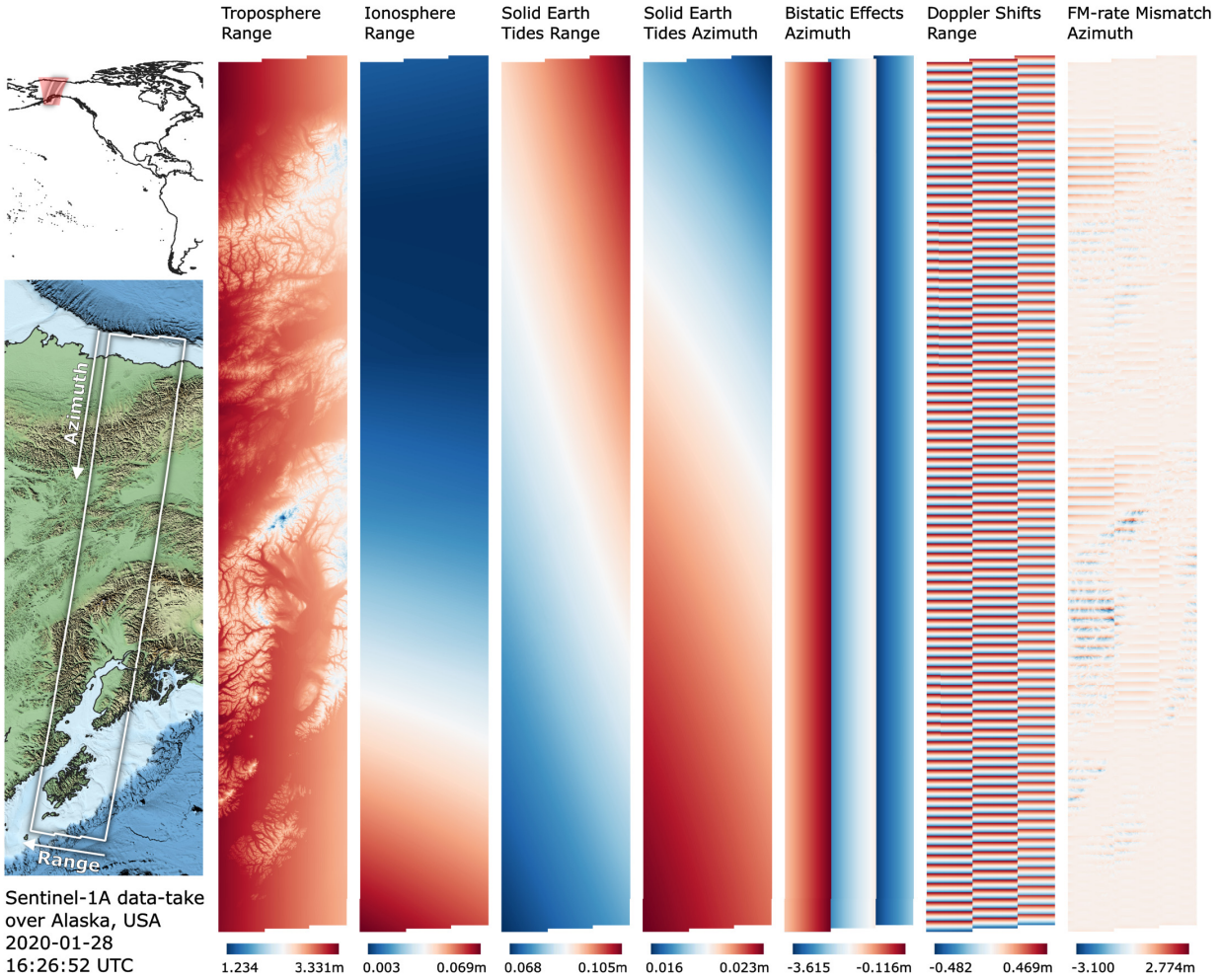

Fig. 3. Visualization of the seven ETAD correction layers contained in the NetCDF product for a S-1A data take acquired over Alaska, USA. Timing corrections converted to units of meters by speed of light in vacuum divided by two (range corrections) and the zero-Doppler beam velocity (azimuth corrections).

rate which is driven by the sensor-to-ground geometry. The range-dependent change is modeled with sufficient detail when defining the matched filter. However, the effective velocity parameter underlying the azimuth FM rate computation is kept constant during the processing of large azimuth blocks. These comprise up to several seconds in azimuth dimension, e.g., the 3 s burst size of S-1 TOPS. While for stripmap SAR with zero-Doppler steering, the effect of mismatch (quadratic phase error, [1]) is mainly a defocussing of the image, there is also a shift in azimuth for TOPS products. Around the borders of mountainous areas, shifts of a few meters can be found at the edge of the burst because the average scene height assumed for FM rate calculation can differ from the local height by thousands of meters.

The azimuth FM rate mismatch correction is computed from the annotated Doppler centroid frequency at the grid location $f_{dc,g}$ and the azimuth FM rate k_a, g applied by the SAR processor. The correction is calculated by considering the difference to the true azimuth FM rate $k_{a,\text{geom}}$ derived from the orbit to grid point geometry

$$\Delta t_{\text{FMM}} = f_{dc,g} \cdot \left(\frac{1}{-k_{a,g}} - \frac{1}{-k_{a,\text{geom}}} \right). \tag{8}$$

The computed corrections show strong variations across affected burst and spatial correlation with topographic features contained in the scene; see Fig. 3.

C. Product Usage

For the application of ETAD timing corrections, the NetCDF product has to be accessed and corrections have to be applied on burst level. To facilitate straightforward data usage, ESA maintains an API to extract burst timing corrections from the NetCDF file [51].

1) Application of ETAD Product to Correct SLC Data Timing: S-1 ETAD gridded corrections are applied to SLC data on a burst-by-burst basis, whose original pixel positions are defined by the annotated time coordinates (t, τ). The time annotated ETAD correction grids have first to be resampled to higher resolution SLC raster by applying a simple bilinear interpolation. This can be performed for any combination of correction grids or most conveniently using the prepared summation grids. The sum of ETAD range corrections $\Delta_\tau(t, \tau)$ and azimuth corrections $\Delta_t(t, \tau)$ is then subtracted from the original SLC slant range and azimuth timings, thus resulting in an irregularly gridded but timing-corrected SLC dataset.

Note that the bistatic azimuth correction (6) and the Doppler shift range correction (7) are annotated in the ETAD product as correction layers with opposite sign, and thus have to be subtracted from the SLC timing annotation as all the other corrections. To resample the corrected and now irregularly spaced raster back to a regular grid, phase preserving complex interpolation has to be used [52], and subsequent processing can continue as normal. For a detailed description of timing corrections of individual targets and S-1 SLC data, the reader may refer to [33]. The application to S-1 ground range, multilook, detected (GRD) products is also possible with some caveats; see [33], but to achieve high timing accuracies we always recommend to correct S-1 SLC data.

2) Application of ETAD Product to Correct Phase: Phase corrections should be calculated from individual $\Delta\tau$ range corrections that are converted into radians. Let λ_{S1} be the wavelength of the sensor and c the speed of light in vacuum

$$\Phi_{\text{ETAD}} = -(\Delta\tau_{\text{tro}} + \Delta\tau_{\text{tides}} - \Delta\tau_{\text{ion}} + \cdots \Delta\tau_{\text{cal}} + \Delta\tau_{\text{pol}}) \cdot \frac{2\pi c}{\lambda_{S1}}. \quad (9)$$

Note the inverse sign for ionospheric phase correction due to the dispersive properties of the ionosphere. The range calibration $\Delta\tau_{\text{cal}}$ and polarization calibration $\Delta\tau_{\text{pol}}$ given in the product annotation only have to be accounted for if interferograms are calculated from S-1A and S-1B combinations or from different polarization channels [33]. Currently, the only missing range correction that is annotated in the ETAD product, the Doppler range shift system correction (see Section II-B5), is omitted from this formula as it is not clear to which extent its effect is already compensated in various interferometric processors.

III. Validation at Geodetic Calibration Sites

A. Sites and Methods

The quality and accuracy of ETAD timing corrections can be validated with S-1 measurements of stable calibration targets with known reference coordinates. For assessing the product, we used triangular trihedral corner reflectors (CRs) with 1.5- m edge length, which are installed at the geodetic stations of Metsähovi (Finland), Wettzell (Germany), and Yarragadee (Australia) [20], [53]. The procedures are well-established and are commonly applied when determining the absolute location error (ALE) of SAR systems [21], [54], [55]. Such studies were also performed by DLR with S-1 data to verify the correction methods, and more details on ALE assessment can be found in [23].

The ALE of an SAR system is determined by comparing reference values for range and azimuth computed from known target position and precise orbit solution with the range and azimuth target coordinates extracted at the subpixel level from SLC SAR images. The comparison has to account for the errors introduced by the atmosphere, the solid Earth deformations, and the SAR processing effects, which allows validation of the corrections offered by the ETAD products. For each SAR image and the corresponding ETAD product, residuals are computed and converted into units of meters as follows:

$$\begin{aligned} \Delta rg &= \left(\tau_{\text{SAR}} - \tau_{\text{ref}} - \Delta\tau_{\text{ETAD,sum},rg}\right) \cdot c/2 \\ \Delta az &= \left(t_{\text{SAR}} - t_{\text{ref}} - \Delta t_{\text{ETAD,sum},az}\right) \cdot v_{\text{beam}} \end{aligned} \quad (10)$$

where τ, t_{SAR} denotes the target coordinates of the SAR image, τ, t_{ref} is the computed reference value, $\Delta\tau_{\text{ETAD,sum},rg}$ and $\Delta t_{\text{ETAD,sum},az}$ are the total sum of ETAD corrections in range and azimuth, respectively, c is the speed of light in vacuum, and v_{beam} is the zero-Doppler beam velocity. The beam velocity of S-1 is in the order of 6800 m/s and is annotated in the ETAD product.

Because ETAD products provide the S-1 precise orbit along with all the corrections' layers, ALE processing becomes straightforward and consists only of the following steps:

1) *Point Target Analysis*: Extraction of the target range and azimuth coordinates from the S-1 SLC SAR image at the subpixel level. A two-step procedure is applied. Spectral zero-padding is used to 32× oversample the complex image data around the peak, followed by the fit of an analytic elliptic paraboloid to define the peak position with a precision better than 1/1000th of a pixel [56].
2) *ETAD Product Evaluation*: Interpolation of the ETAD product range and azimuth summation layers (see Section II-C1) for the obtained range and azimuth coordinate location.
3) *Reference Value Determination*: Computation of reference zero-Doppler range and azimuth coordinates from the precise orbit embedded in the ETAD product and the known ITRF reference coordinates of the target, using the SAR range–Doppler equations in the zero-Doppler configuration (1)(2).
4) *ALE Analysis*: Comparison of the extracted and computed range and azimuth coordinates, considering the corrections; see (10).

The procedure is performed individually for each S-1 SLC SAR and ETAD product, which yields sets of residuals for each calibration site and for both the instruments S-1A and S-1B. The results can be analyzed with respect to:

1) Standard deviations in range and azimuth (product precision, sensor noise)
2) Remaining offsets in range and azimuth (product accuracy, sensor biases)
3) Consistency of S-1A and S-1B when applying the ETAD product (S-1 system performance)
4) Consistency of results regarding ascending and descending passes at the same site
5) Performance of system corrections for CRs located in burst or swath overlap areas

The calibration sites hosting the trihedral CRs are described in Table III. Each of the geodetic observatories provides one or two permanently installed CR that are attached either to a deep concrete foundation or directly to stable bedrock. The sites have been measured with terrestrial geodetic surveys with a 3-D precision of better than 5 mm (Wettzell, Metsähovi) and better than 10 mm (Yarragadee). The coordinates were accurately transformed to the global ITRF 2014 at reference epoch 2010, applying the station's known local network to

TABLE III
SUMMARY OF GEODETIC CALIBRATION SITES EQUIPPED WITH TRIHEDRAL CORNER REFLECTORS

Calibration Site	**Site Location** (latitude/longitude)	**SAR Ground Infrastructure**	**Description**
Metsähovi Geodetic Observatory	Finland (60.2176 °/24.3945 °)	1.5 m CR (1)	CR facing East (S-1 descending tracks); Reference coordinates from terrestrial local tie survey ($< 5\,\mathrm{mm}$)
Wettzell Geodetic Observatory	Germany (49.1447 °/12.8783 °)	1.5 m CR (2)	CRs facing East and West (S-1 ascending and descending tracks); Reference coordinates from terrestrial local tie survey ($< 5\,\mathrm{mm}$)
Yarragadee Geodetic Observatory	Australia (-29.0474 °/115.3461 °)	1.5 m CR (2)	CRs facing East and West (S-1 ascending and descending tracks); Reference coordinates from terrestrial local tie survey ($< 10\,\mathrm{mm}$)

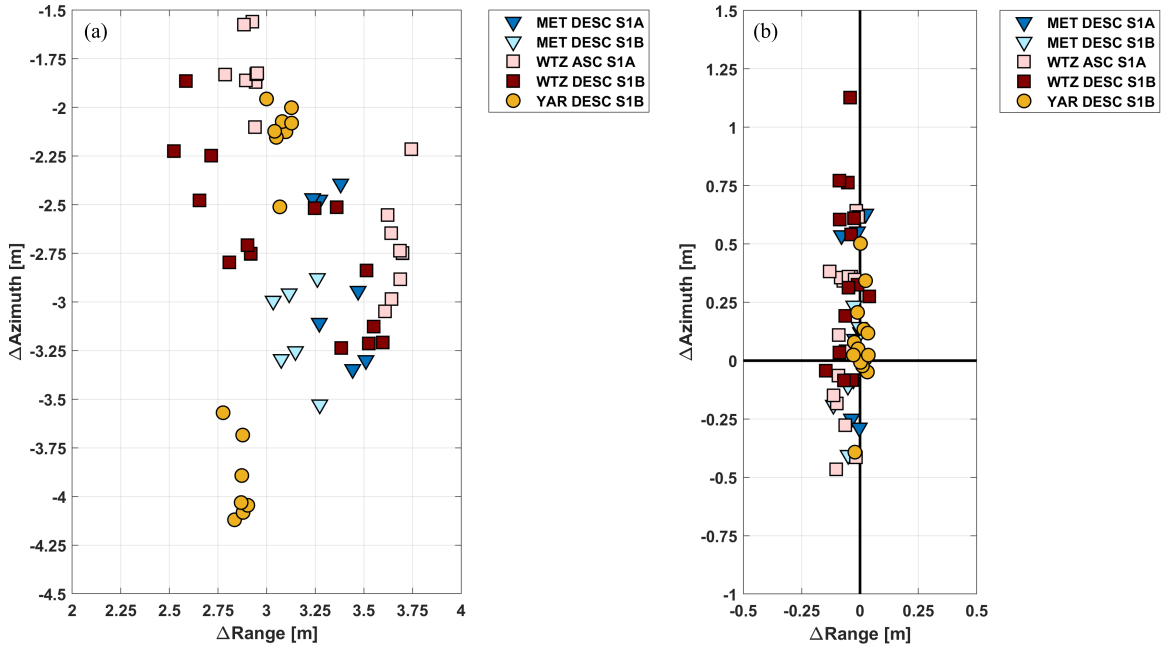

Fig. 4. Geolocation residuals obtained with S-1 IW data for different test sites. Raw results without applying corrections (a) and results when applying the ETAD product (b). Note the different axis scaling.

TABLE IV
SUMMARY OF S-1 DATA AND ETAD PRODUCTS USED FOR VALIDATION AT THE CALIBRATION SITES

Site / Pass	**Sensor**	**Relative Orbit Nr.**	**Mode**	**Pol.**	**No. of Products**	**Remarks**
Metsähovi / DESC 1	S-1A	51	IW	VV, VH	7	
Metsähovi / DESC 2	S-1B	153	IW	VV, VH	6	
Wettzell / ASC	S-1A	44	IW	VV, VH	8	CR located in burst overlap
Wettzell / DESC	S-1B	95	IW	VV, VH	7	CR located in burst overlap
Yarragadee / ASC	S-1B	25	SM	HH	18	
Yarragadee / DESC	S-1B	61	IW	VV, VH	8	CR located in swath overlap

ITRF transformation parameters [57]. The test data for this validation activity consist of S-1 data acquired between August 2019 and August 2020 for which the ETAD products have been computed; see Table IV. The IW data cover a period of three months in summer 2019 to avoid any deterioration due to snow in the CRs. This yields 7–8 ETAD products per site and

TABLE V

GEOLOCATION RESULTS (MEAN ± STANDARD DEVIATION) OBTAINED WITH IW DATA FOR DIFFERENT TEST SITES. ABSOLUTE LOCATION ERROR (ALE) WITHOUT APPLYING CORRECTIONS (RAW) AND AFTER APPLYING THE ETAD PRODUCT (ETAD)

Calibration Site & Sensor	Range ALE [m]		Azimuth ALE [m]	
	RAW	ETAD	RAW	ETAD
Metsähovi DESC S-1A	3.369 ± 0.110	-0.023 ± 0.032	-2.862 ± 0.412	0.170 ± 0.397
Metsähovi DESC S-1B	3.151 ± 0.098	-0.041 ± 0.042	-3.151 ± 0.249	-0.034 ± 0.243
Wettzell ASC S-1A	3.287 ± 0.394	-0.066 ± 0.038	-2.267 ± 0.522	0.125 ± 0.351
Wettzell DESC S-1B	3.092 ± 0.400	-0.054 ± 0.043	-2.695 ± 0.418	0.381 ± 0.369
Yarragadee DESC S-1B	2.968 ± 0.117	0.005 ± 0.021	-3.032 ± 0.951	0.064 ± 0.190
Total S-1A & S-1B	3.150 ± 0.320	-0.036 ± 0.045	-2.736 ± 0.687	0.159 ± 0.334

configuration, which have a temporal sampling of 12 days. SM data at Yarragadee were specifically acquired with a 24-day repeat interval for one year, and all the available products are used for verification.

B. Geolocation Results for IW Products

Without applying any corrections, the ALE residuals of S-1 IW data show typical systematic effects which are caused by different types of errors stemming from physical effects (atmosphere, solid Earth tides) and S-1 SAR system effects; see Fig 4(a) and RAW ALE results in Table V.

The range residuals are dominated by the approximately 3- m bias of tropospheric delay, as well as Doppler range shifts not corrected in the S-1 level 1 products, which are clearly visible in the results of CRs situated in burst and beam overlaps: WTZ ascending (ASC), WTZ descending (DESC), and YAR DESC. Despite having been observed with the same atmospheric conditions, the residuals of these three calibration targets become divided into two groups that belong to different overlapping bursts.

The azimuth ALE residuals are driven by the bistatic azimuth effects only partly compensated for in processed S-1 level 1 data [23], [58]. The impact is most prominent in the results of YAR DESC where the measurements are performed in overlapping beams (IW1, IW2). The azimuth results are separated by approximately 2 m because of the interbeam bistatic biases. In summary, the uncorrected data yield a combined S-1 ALE result of 3.15 ± 0.32 m in range and -2.75 ± 0.69 m in azimuth; see Table V. These findings are in perfect agreement with our earlier results obtained with S-1A and S-1B at the Australian CR array [23].

After applying the corrections from the ETAD product, the impact of the effects discussed above is greatly reduced. The range ALE offsets and standard deviations are now at a level of a few centimeters, showing only minor differences between different stacks, calibration sites, and S-1A and S-1B sensors (Table V, Fig. 4(b)). The azimuth ALE results show a similar improvement in eliminating the systematic discrepancies. However, after correcting all the timing errors, the geolocation precision becomes limited by the approximately 22- m azimuth resolution of the IW SLC data [31], which impacts measurement accuracy because of the signal to clutter ratio (SCR) of the used CRs. For the trihedral triangular CRs with 1.5- m edge length, the average SCR observed with the IW data is 22 dB, which translates into a theoretical azimuth precision ($1\,\sigma$) of 0.68 m when applying the error estimation assuming uncorrelated clutter [59]. In fact, our measurements are better than this prediction which may be caused by the overestimated clutter or by correlated background clutter [60], but an overall SCR limitation is still manifested in the standard deviation of the azimuth residuals list in Table V. Nevertheless, the azimuth ALE of IW data benefits from the ETAD system corrections which enable comparable observations across different test sites.

C. Geolocation Results for SM Products

With an average resolution of 2.5 m in range and 4.5 m in azimuth [31], the S-1 SM data have considerably higher azimuth resolution than IW data, and therefore the attainable geolocation accuracy is higher as well because of the increase in target SCR and resolution. The uncorrected SM data show an azimuth offset due to the bistatic error and a range offset mainly caused by the tropospheric delay; see Fig. 5(a) and RAW ALE results in Table VI. The additional spread in range is caused by the atmosphere and solid Earth tides.

The results for the corrected data are shown in Table VI and Fig. 5(b). The corrections from the ETAD product remove the range bias and improve the range ALE standard deviation from 0.14 m to 0.02 m at the given test site. The range data become almost perfectly centered which confirms the consistency of the IW and SM range observations of S-1 when applying ETAD corrections. In the ETAD product, the azimuth SM data are only corrected for the bistatic effect, which is mainly a bias, and the horizontal solid Earth tide deformations, which at the given site are at the ± 0.03 m level. Consequently, there is only a small improvement in the standard deviation; see Table VI, whereas the azimuth bias is largely removed.

Overall, centering of the data is achieved with the ETAD timing calibration, which was determined for IW data (see Section II-A). The results show that for range data the correction is already well-defined, but for azimuth SM data there remains an offset of 0.15 m. Therefore, a refinement of the timing calibration auxiliary dataset used by ETAD (see Section II-B) has to be performed to adjust the SM geolocation accuracy in azimuth.

TABLE VI

GEOLOCATION RESULTS (MEAN ± STANDARD DEVIATION) OBTAINED WITH SM DATA AT THE YARRAGADEE TEST SITE. ABSOLUTE LOCATION ERROR (ALE) WITHOUT APPLYING CORRECTIONS (RAW) AND AFTER APPLYING THE ETAD PRODUCT (ETAD)

Calibration Site & Sensor	Range ALE [m]		Azimuth ALE [m]	
	RAW	ETAD	RAW	ETAD
Yarragadee ASC S-1B	3.318 ± 0.142	0.011 ± 0.020	-2.093 ± 0.048	0.157 ± 0.046

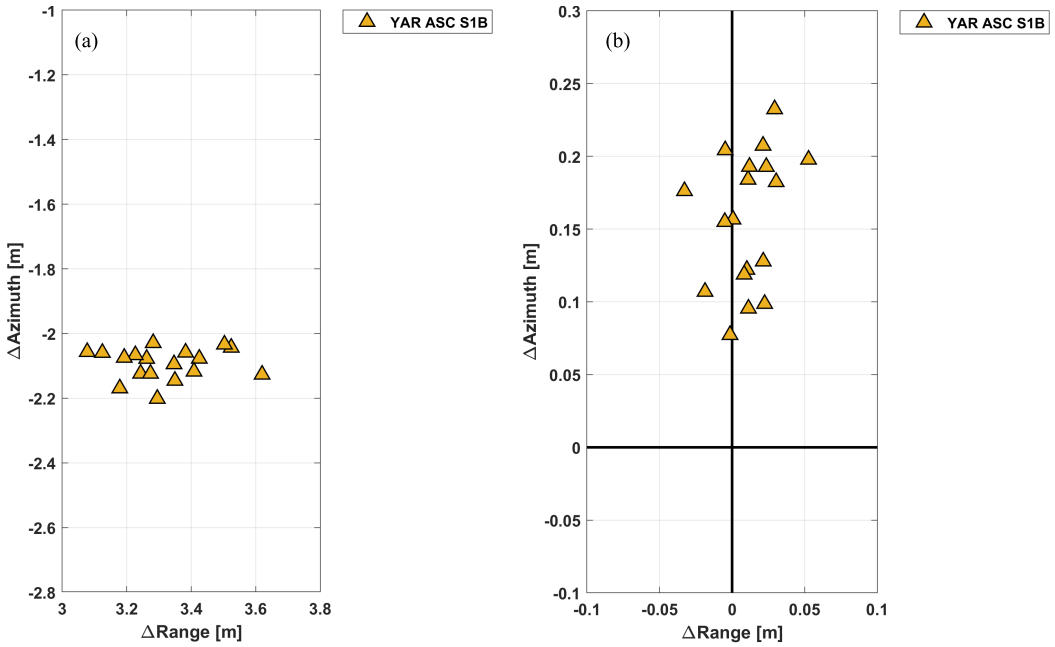

Fig. 5. Geolocation residuals obtained with S-1 SM data for the Yarragadee test site. Raw (a) results without applying corrections and (b) results when applying the ETAD product. Note the different axis scaling.

D. Discussion of Geolocation Results

The geolocation range results obtained with the ETAD product are well within the range correction specifications (see Section II-A). The range accuracy achieved with IW data across all the tests with different beams and sensors is better than 0.05 m and even better (0.02 m) for SM range data. The azimuth geolocation, however, is limited by effects beyond the scope of the ETAD product. Whereas the results achieved with SM data show a very high geolocation precision of 0.05 m in azimuth that is clearly within ETAD specification, the geolocation precision obtained with IW data is 0.3 m due to the coarser azimuth resolution and the limited SCR of the CRs. We have no reason to assume that the ETAD azimuth corrections for IW are worse than those for SM. Moreover, both the modes show a systematic azimuth offset of about 0.15 m.

These remaining errors are the combined effect of orbit accuracy, uncompensated sensor biases, and the impact of SCR versus resolution of the SAR image product:

1) The accuracy of the S-1 precise orbit product is better than the required 5 cm 3-D rms [13].
2) For the processed IW data, the SCR of the CRs reads 22 dB which translates into a theoretical geolocation precision of ±0.09 m (range) and ±0.68 m (azimuth) when applying the average S-1 IW image resolution of 3 m (range) and 22 m (azimuth) [31], [59].
3) For the processed SM data, the SCR of the CRs reads 28 dB which translates into a theoretical geolocation precision of ±0.04 m (range) and ±0.06 m (azimuth) when applying the average S-1 SM image resolution of 2.5 m (range) and 4 m (azimuth) [31], [59].
4) The biases stem from S-1 sensor characteristics, system aging, and other unknown effects that have to be calibrated for the system.

Considering the impact of SCR, the ETAD products perform to specification and the accuracy can be ensured by refining the sensor timing calibration used by the ETAD processor; see the outlook in section VI. In summary, the performed ETAD product validation confirms that the product behaves as expected, and the geometric accuracy attainable at global scale with S-1 data is now at least 0.2 m in range and 0.1 m in azimuth.

IV. ICE VELOCITY MONITORING IN GREENLAND

The ice flow of the Greenland ice sheet is routinely monitored by ENVEO through Copernicus Climate Change Service (C3S) for Land Hydrology and Cryosphere [61]. In this operational framework, ice velocity (IV) is mapped by applying the

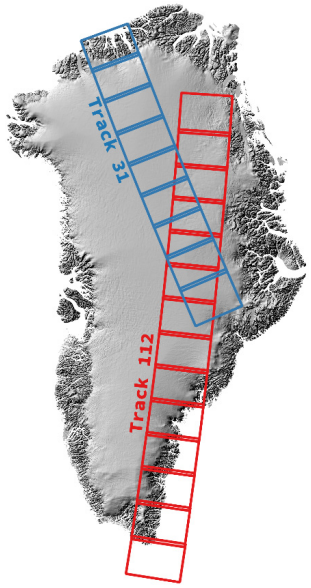

Fig. 6. Coverage of S-1 Greenland IV data: track 31 (blue) and track 112 (red).

well-established SAR OT technique to each 6-day and 12-day pair of S-1 SLCs acquired over Greenland [27].

The OT technique consists in determining the local misalignment between repeat pass SAR images by finding the maximum of the cross correlation peak that corresponds to the offset [24]–[26], [62]–[64]. When OT is applied to ice sheets or glaciers and if SAR images are geometrically coregistered beforehand, the estimated offsets can be assumed to be directly related to ice motion. In practice, amplitude-based OT uses SAR amplitude images as templates to determine displacements of ice surface features such as crevasses, rifts, or edges. In case speckle is coherent, it can provide even higher accuracy than features. OT estimates displacements in both the range and azimuth directions, which are subsequently normalized by the temporal baseline to obtain velocity measurements. One of the main error sources is uncompensated propagation delays, in particular the tropospheric and ionospheric ones, which are in turn misinterpreted as ice motion. To correct for such biases, OT results are usually calibrated against stable or slow-moving areas (e.g., rocks or ice divides) in a postprocessing step. However, calibration can turn out to be challenging in regions lacking stable areas and *in situ* measurements, e.g., for tracks covering only the interior of the ice cap. In this case, ETAD products provide a valuable alternative. In this section, the use of timing delay corrections as provided by ETAD products is investigated for compensating biases in OT IV measurements.

A. Methods

In the case of OT, we consider two approaches to compensate timing delays by applying ETAD corrections: the first approach is the SLC timing correction of individual SAR images before processing, which is described in Section II-C1; the second approach is a postprocessing bias correction of local pixel shifts estimated between two SAR SLC images. The SLC timing correction is of interest if one has to process the same SLCs with multiple techniques; for processing a dataset with OT only, or for correcting archive results, the second method is faster and computationally less expensive. In both the cases, the ETAD correction module can be easily integrated to standard processing chains.

As explained in Section II-C1, the use of ETAD for correcting SLC timing enables to resample each pixel to its accurate position in the SAR image by correcting timing errors of various origins. The ETAD SLC timing correction must be applied to both the reference and secondary SLCs used for OT. The output products are timing-corrected SLCs, directly ingested into the standard OT processing chain. This method is expensive because resampling has to be performed on complex images at full resolution on aliased TOPS data, i.e., at nonzero-Doppler frequencies. The interpolator must be capable to handle very small shifts of less than 1/100 of a pixel. Moreover, it doubles the storage space of the SLC data, which can become critical for wide-scale monitoring. The second approach requires no interpolation of SLC data as it applies the corrections directly on the shift vectors derived from OT.

Let us consider that the offset-tracking range and azimuth velocity estimates v_{rg}^{OT} and v_{az}^{OT} are already available for a given pair of uncorrected reference and secondary SLC. Then the postprocessing bias correction consists of: 1) upscaling the reference and secondary ETAD timing delays to the SLC grid multilooked at the OT grid resolution using a bilinear resampling, 2) resampling the secondary ETAD to the reference OT geometry, and 3) correcting the offset-tracking velocity estimates according to

$$v_{rg}^{OT'} = v_{rg}^{OT} - \frac{\left(\Delta\tau_{\mathrm{ETAD,sum},rg}^{\mathrm{ref}} - \Delta\tau_{\mathrm{ETAD,sum},rg}^{\mathrm{sec,res}}\right)}{\Delta T} \cdot \frac{c}{2} \quad (11)$$

$$v_{az}^{OT'} = v_{az}^{OT} - \frac{\left(\Delta t_{\mathrm{ETAD,sum},az}^{\mathrm{ref}} - \Delta t_{\mathrm{ETAD,sum},az}^{\mathrm{sec,res}}\right)}{\Delta T} \cdot v_{\mathrm{beam}} \quad (12)$$

where $v_{rg}^{OT'}$ and $v_{az}^{OT'}$ are the corrected OT velocity estimates in the range and azimuth directions, respectively, ΔT is the temporal baseline between the reference and secondary acquisitions, $\Delta\tau_{\mathrm{ETAD,sum},rg}^{\mathrm{ref}}$ and $\Delta\tau_{\mathrm{ETAD,sum},az}^{\mathrm{ref}}$ are the upscaled sums of ETAD range and azimuth timing corrections corresponding to the reference acquisition, respectively, $\Delta\tau_{\mathrm{ETAD,sum},rg}^{\mathrm{sec,res}}$ and $\Delta\tau_{\mathrm{ETAD,sum},az}^{\mathrm{sec,res}}$ are the upscaled and resampled sums of ETAD range and azimuth timing corrections corresponding to the secondary acquisition, respectively, c is the speed of light, and v_{beam} is the zero-Doppler beam velocity. This calculation is performed pixel-wise, and the position indices have been omitted for the sake of readability.

The postprocessing ETAD correction is operated at multilooked resolution and has therefore reduced computational and storage costs compared with SLC timing correction. It also opens the possibility to correct archive results without the need of a full reprocessing. The SLC timing corrections are still worth considering the case of multiapproaches studies. Both the approaches are evaluated in the following using the dataset described below.

B. Dataset and Processing

For testing the OT IV bias compensation, the two methods are tested on a dataset of S-1 SLCs acquired over Greenland.

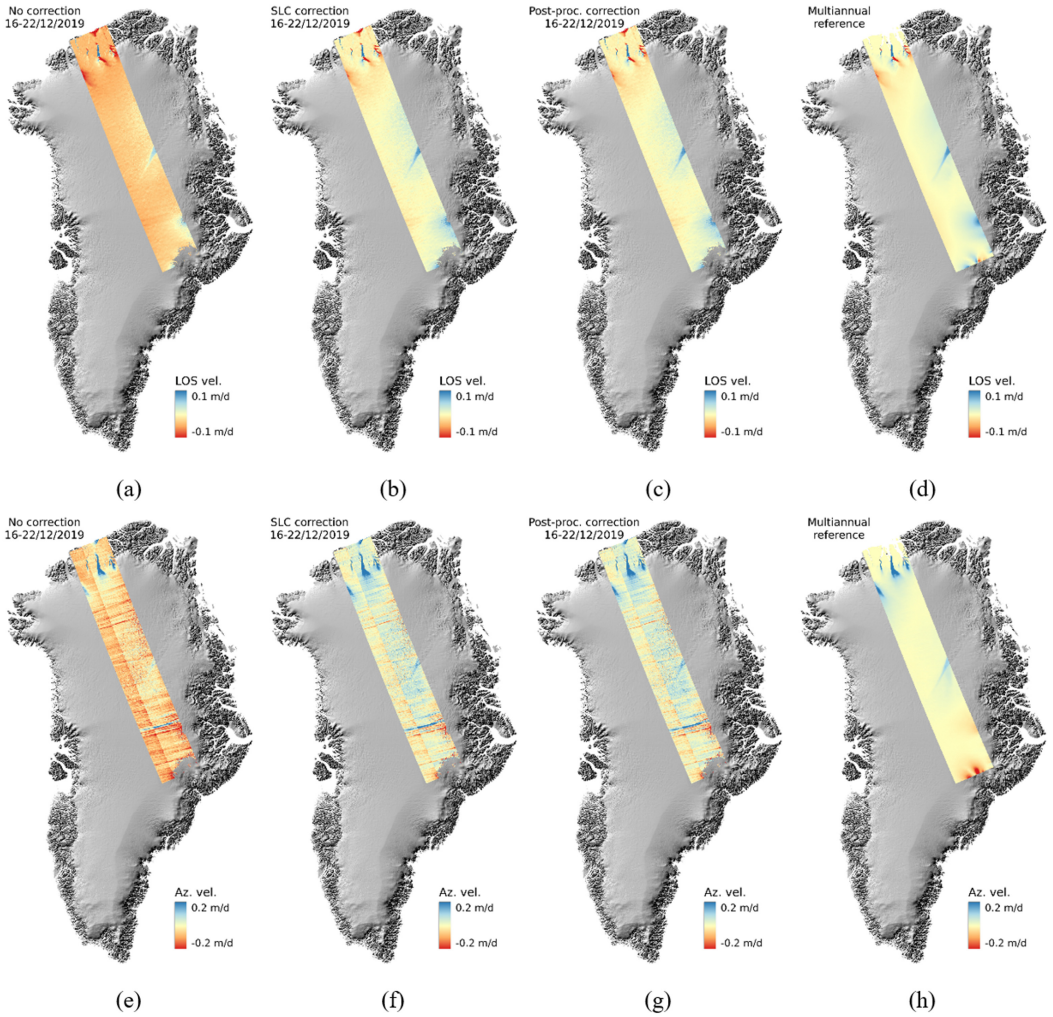

Fig. 7. (a)–(d) Range and (e)–(h) azimuth velocity components measured with (a) and (e) uncorrected OT, (b) and (f) OT with SLC timing corrections, (c) and (g) OT with postprocessing corrections and compared with (d) and (h) multiannual velocity reference. OT is applied to a 6-day S-1A and S-1B pair acquired along track 31 (16/12/2019–22/12/2019).

TABLE VII
DESCRIPTION OF SENTINEL-1 DATASET USED FOR THE GREENLAND EXPERIMENT

Pass	Sensor	Relative Orbit Nr.	Mode	Pol.	Products
ASC	S-1A	31	IW	HH	16/12/2019
					28/12/2019
ASC	S-1B	31	IW	HH	22/12/2019
DESC	S-1B	112	IW	HH	16/12/2019
					28/12/2019

ETAD products have been computed for each acquisition of the dataset described in Table VII. The dataset consists of long stripes of S-1 IW SLC data acquired along the ascending and descending tracks with 6- and 12-day repeat during winter 2019. These tracks cover at the same time fast ice streams the slow-moving ice sheet interior and stable rocks on the coast; see Fig. 6. The tracks, the coverage, and the repeat interval (6 and 12 days) are representative of the operational scenario used in the C3S IV monitoring service [61].

For each possible pair of acquisitions, OT is applied without bias compensation, with ETAD SLC timing corrections, and with ETAD postprocessing corrections. Range and azimuth velocities are calculated on a grid multilooked on 40 × 20 pixels in the range and azimuth directions, respectively, filtered and eventually geocoded on a 100- m grid with polar stereographic projection. Measurements with a cross-correlation below 0.1 are dismissed. Processing parameters are kept constant for all the methods. For validation, the results are compared with a multiannual reference IV map generated with OT. The reference map is the solution of a least-squares problem made up of more than five years of S-1 OT measurements, each individual 6- and 12-day OT results being calibrated against stable and slow-moving areas. This reference map is hence representative of the stable state of the Greenland ice sheet. During winter, little ice flow variations are expected, and OT IV measurements should hence be as close as possible to this reference.

C. Results and Discussion

The performance of ETAD corrections can be qualitatively appreciated by comparing the multiannual IV reference with the OT IV results without bias compensation, with ETAD SLC timing correction, and with ETAD postprocessing correction, as shown in Fig. 7 for a 6-day pair involving S-1A and S-1B. The uncorrected velocities show an obvious error for the range and azimuth components when compared with the reference solution. In particular, the velocity differs from zero on the coast, where the rocks are free of ice and nonmoving. In addition to the large-scale error, the azimuth component also suffers from local ionospheric streaks. Ionospheric streaks are shifts in the azimuth position caused by kilometer-scale disturbance of the ionosphere electron content [65]. They are commonly observed for OT processing in the polar regions and remain challenging to correct. Both the ETAD SLC timing correction and the ETAD postprocessing bias correction efficiently remove undesired large-scale trends and intersensor biases, showing velocity estimates close to zero on rocky areas. However, due to the coarser natural resolution of the underlying ionospheric data compared with the scale of such local ionospheric disturbances, and the omission of ionospheric corrections for azimuth timings in ETAD products (see Section II-B2), the streaks remain uncorrected for the azimuth component.

For assessing quantitatively the performance of the correction approaches, we compute the difference between the reference velocity and the OT measurements for each pair and each method. This deviation with respect to the reference velocity is referred to as the velocity residual and is calculated pixel-wise for the range and azimuth components. A typical distribution of these residuals with and without ETAD corrections is shown in Fig. 8 for a 6-day pair and a 12-day pair. The ETAD postprocessing corrections yield results practically identical to SLC timing corrections and are hence not displayed in this figure. Both the range and azimuth components appear to be normally distributed. Residuals of the azimuth components have a larger spread than those of the range components, due to the ionospheric streaks introducing local errors that cannot be corrected with ETAD. In the 6-day case, the residuals of the uncorrected OT results are distributed around a nonzero center value for the range and azimuth components (about 0.035 m/day and 0.065 m/day, respectively). Applying SLC timing corrections, the distribution is shifted toward zero and the bias is significantly reduced to approximately 0.002 m/day and 0.01 m/day in range and azimuth, respectively.

However, for the 12-day example, the bias is smaller and the improvement is therefore less significant. For the range component, the distribution is still shifted by about 0.004 m/day toward zero, but for the azimuth component, the shift is smaller than 1 mm/day and the uncorrected and corrected residual distributions overlap. The reduced improvement in the 12-day case is expected as the OT measurements are usually less biased for longer temporal baseline, because: 1) OT has a better sensitivity to large displacements; 2) the displacements measured with OT are normalized by the temporal baseline to calculate velocities, and the contribution of the path delay therefore decreases as the temporal baseline increases, making 12-day pairs less affected by timing errors than 6-day pairs. The scaling by the temporal baseline should in theory yield an accuracy of 12-day OT results better than the 6-day case by a factor 2, although a larger amount of scenes would be necessary to prove it.

For all the four analyzed pairs and both the corrections methods, the average residual values and their standard deviations are listed in Table VIII. As already observed with the histograms, for 6-day pairs, the average residual bias improves from a few centimeters per day in the uncorrected case to less than 1 cm/day with the ETAD, and even better in some cases. The standard deviation remains mostly unchanged when ETAD corrections are applied. The small residuals obtained when ETAD corrections are applied highlight the reduced need for velocity calibration that is required in the uncorrected case. Furthermore, the improvement is similar for SLC timing corrections and postprocessing bias corrections, both the methods being therefore considered equivalent.

Due to the bias being smaller in the 12-day case, the improvement provided by ETAD correction is strongly reduced. The particular pair over track 112 even shows slightly worsened measurements when ETAD corrections are applied. The performance of ETAD correction in this particular example must, however, be put in perspective, considering that 1) track 112 crosses a region of high accumulation located on the southeastern coast of Greenland, where correlation is reduced and errors might be introduced, while the situation might be improved locally in some other places; 2) the mean correction and the mean residual velocity are subcentimetric, which is at the edge of OT noise floor and thus making variations in the residuals between the uncorrected and corrected cases of little significance [24], [59]. Furthermore, the combination of high accumulation, causing inaccuracies in the velocity measurements, associated with a wide variety of velocities in the scene leads to overall larger standard deviations of the residuals compared with the other examples.

V. InSAR Applications in Norway

The most significant noise source in InSAR time series analysis is the spatially varying and strongly time-dependent delay through the atmosphere, see for instance [66], [67]. The atmospheric phase screen (APS) present in interferograms consists of a topography-dependent part and a topography-independent part [68]. It has been demonstrated that the topography-dependent component of the atmospheric phase screen may be reasonably predicted under certain conditions using only SAR data [69], or using auxiliary numerical weather models [70]. The topography-independent part can be further decomposed into a relatively stable part over long spatial scales ($>$50 km) and a part due to turbulent mixing with shorter spatial and temporal scales [7]. While the turbulent part of the atmospheric signal is not easily predictable, the components of spatial scales larger than about 50 km are typically captured well by NWMs.

A. Benefit of ETAD for InSAR

It is challenging to compensate for the APS present in SAR data [68]. Most mitigation approaches rely on assumptions

TABLE VIII

RANGE AND AZIMUTH AVERAGE VELOCITY RESIDUALS FOR EACH PAIR OF THE TEST DATASET. AVERAGE RESIDUALS ARE OBTAINED WITH A SPATIAL MEAN AND PROVIDED FOR: OT WITH NO CORRECTIONS, WITH SLC TIMING CORRECTION, AND WITH POST-PROCESSING CORRECTION ALONG WITH THE STANDARD DEVIATION

S-1 pair	Orbit Nr.	ΔT (days)	Spatial average of LOS velocity residuals (m/day)			Spatial average of azimuth velocity residuals (m/day)		
			No correction	SLC correction	Post-proc. correction	No correction	SLC correction	Post-proc. correction
16/12/2019 - 22/12/2019	31	6	0.036 ± 0.008	0.002 ± 0.008	0.002 ± 0.008	0.063 ± 0.057	-0.009 ± 0.057	-0.012 ± 0.057
22/12/2019 - 28/12/2019	31	6	-0.025 ± 0.007	-0.001 ± 0.007	-0.001 ± 0.007	0.069 ± 0.048	0.004 ± 0.048	0.006 ± 0.048
16/12/2019 - 28/12/2019	31	12	0.005 ± 0.007	0.001 ± 0.007	0.001 ± 0.007	-0.001 ± 0.031	-0.001 ± 0.031	-0.001 ± 0.031
16/12/2019 - 28/12/2019	112	12	-0.004 ± 0.093	-0.006 ± 0.091	-0.006 ± 0.093	-0.001 ± 0.170	-0.003 ± 0.168	-0.003 ± 0.170

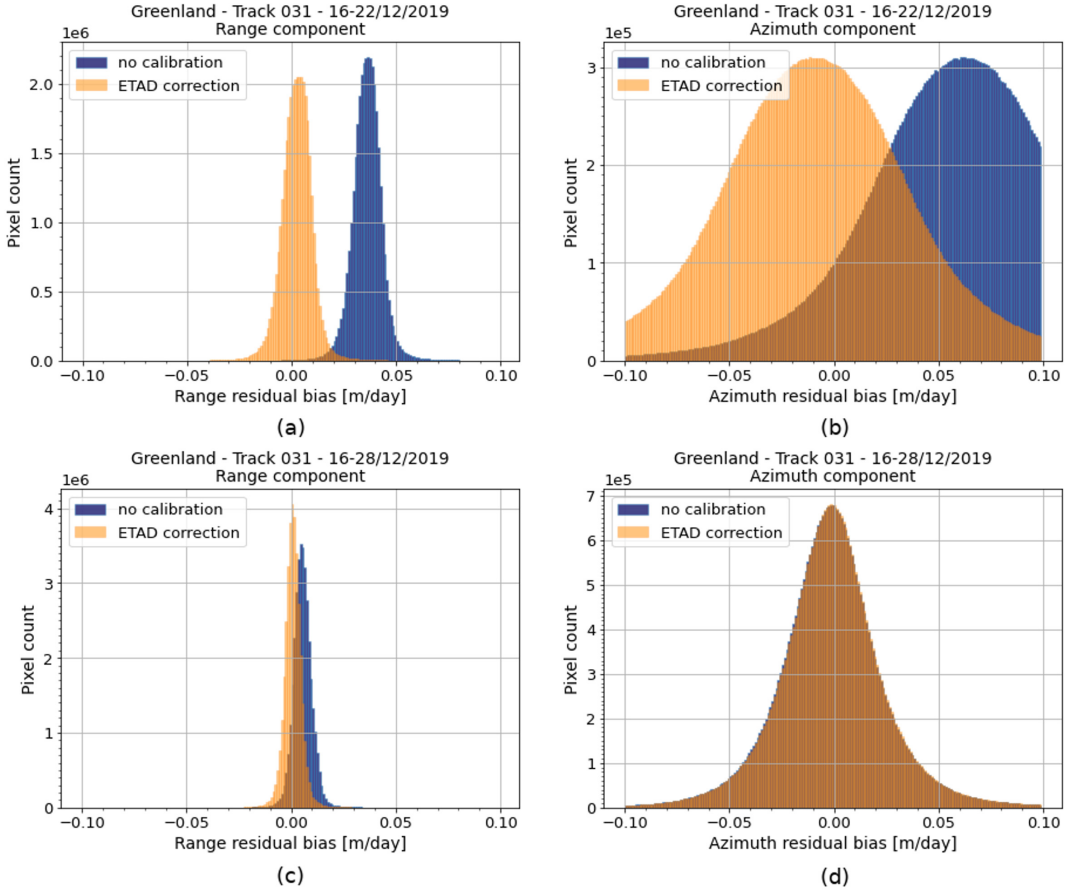

Fig. 8. Histogram of range and azimuth OT velocity residuals for 6- and 12-day pairs (track 31), with (orange) and without (blue) ETAD SLC timing corrections. Residuals are computed as the difference in the OT results compared with the multiannual velocity reference. (a) 16/12/2019–22/12/2019—range velocity residuals. (b) 16/12/2019–22/12/2019—azimuth velocity residuals. (c) 16/12/2019–28/12/2019—range velocity residuals. (d) 16/12/2019–28/12/2019—azimuth velocity residuals.

about the statistical behavior of APS in space and time [66]. In particular, the APS is assumed to be smooth in the spatial domain and decorrelated from acquisition to acquisition in the temporal domain. The latter assumption allows robust mitigation of the APS component due to turbulent mixing in a purely data-driven manner. However, methods such as persistent scatterer interferometry or differential InSAR, e.g., [71], [72], usually perform well only on spatial scales up to a few tens of kilometers [73].

The long spatial scales and the topography-dependent components are often still partially present after data-driven APS mitigation. This typically happens in areas with complex

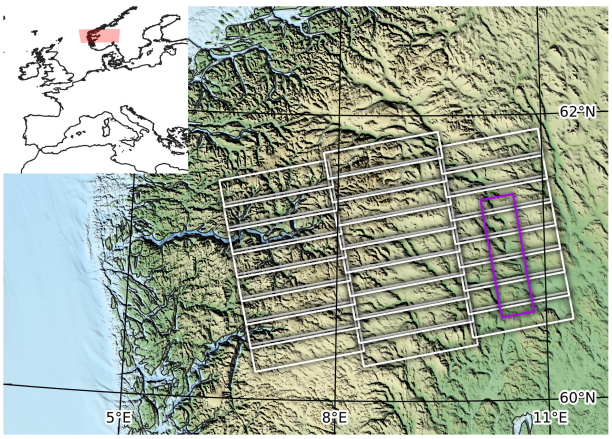

Fig. 9. Overview of area of interest (AOI) for InSAR study with "valley sub-AOI" indicated.

topography, since the statistical assumption used in the estimation of APS is not entirely accurate. While purely data-driven mitigation methods do exist, any reliable and operationally available *a priori* information that can support mitigation of the nonturbulent components is very valuable. Note that due to the turbulent components of APS, ETAD is a supplement to data-driven mitigation, not a replacement.

The ETAD product contains a dedicated layer, based on numerical weather models (Section II-B), for compensation of the atmosphere in S-1 SAR data. In this case study, effectiveness of the ETAD product for mitigation of nonturbulent APS components is evaluated.

B. Site: Norwegian Fjords and Mountains

Several studies [7], [74] have demonstrated the potential of NWM data for robust mitigation of nonturbulent APS components under favorable conditions. In this case study, the performance of such an approach is evaluated in a very challenging area in Southern Norway. The area is characterized by fjords, deep valleys, and complex topography in general. On the other hand, the amount of water vapor in the troposphere is relatively limited, potentially allowing reliable modeling of atmospheric effects. Fig. 9 shows the location of the test area and the outline of the available ETAD products for S-1 ascending track 44. Due to long periods of seasonal snow cover in Scandinavian mountains, only data between June and October are useful for InSAR analysis in this area. For this case study, ETAD products for a stack of 12 S-1 slices from the period July 2–September 6, 2019 and involving S-1A and S-1B were used.

For qualitative evaluation of the performance of stratification correction provided by ETAD, the area of interest is further restricted to a single long and relatively deep valley in the southeastern part of the dataset. The valley Gudbrandsdalen is about 230 km long, and it is typically 10 km wide and 500-800 m deep in the narrower parts, where stratification is most pronounced. The area of interest covers the southern half of the valley. The reduced area of interest is also indicated in Fig. 9.

C. Data Processing

Quantitative and qualitative performance analyses of the ETAD layers for interferometric time series applications were approached as follows:

1) Generate stack of differential Sentinel-1 IW mode burst interferograms, all 66 possible combinations.
2) Multilook the stack of interferograms to approximately the resolution of ETAD products (51 × 15 looks)
3) Mosaic burst interferograms to full slice interferograms
4) Unwrap interferograms
5) Calculate differential range delay correction, (9), from ETAD and resample to the interferogram grid.
6) Compensate unwrapped interferograms by applying ETAD correction and convert to units of range delay in millimeters.

Steps 1–4 are standard Differential InSAR processing steps for the stacks of S-1 data, resulting in 66 unwrapped interferograms for the given stack, and ETAD correction is generated and applied in Steps 5 and 6. An example for the performed processing is shown in Fig. 11.

D. Results and Discussion

To evaluate the performance of ETAD corrections for compensation of long spatial scale components of APS, we apply a variogram analysis to all available interferograms before and after correction, similar to [74].

Fig. 10 shows the results of the performed variogram analysis of all the 66 interferograms. The gain profile in the lower panel shows that the spatial variance drops significantly for scales larger than 25 km, indicating that ETAD corrections in general effectively removed the APS on long spatial scales. On the other hand, a slight average performance loss (∼10 %) can be observed for spatial scales shorter than 25 km. This could be caused by the limited 200- m resolution of the ETAD product, which may lead to nonoptimal corrections in mountainous terrain. A future ETAD product with add-ons for phase corrections in mountains could improve this significantly. Given the typical magnitude of the nonpredictable turbulent mixing component in this challenging area, this is expected and not critical since straightforward data-driven APS mitigation methods perform well on these spatial scales.

It is important to note that the variogram gain shown in Fig. 10, lower panel, is a relative measure, and thus only a relevant measure of success in cases where long spatial scale components and/or stratification are present in the uncorrected interferograms. For interferograms completely dominated by turbulent components, the gain profile will typically be relatively flat and slightly positive, i.e., the errors of NWM would add to the atmospheric phase screen.

In summary, we observe a 3- dB improvement in precision at 100 km distances. While for example, with a simple data stacking approach, four independent interferograms would be required to achieve the same level of improvement, i.e., a factor of 2 lower standard deviation. Therefore, it can be stated that ETAD correction may allow for faster detection of transient deformation because less temporal averaging is required.

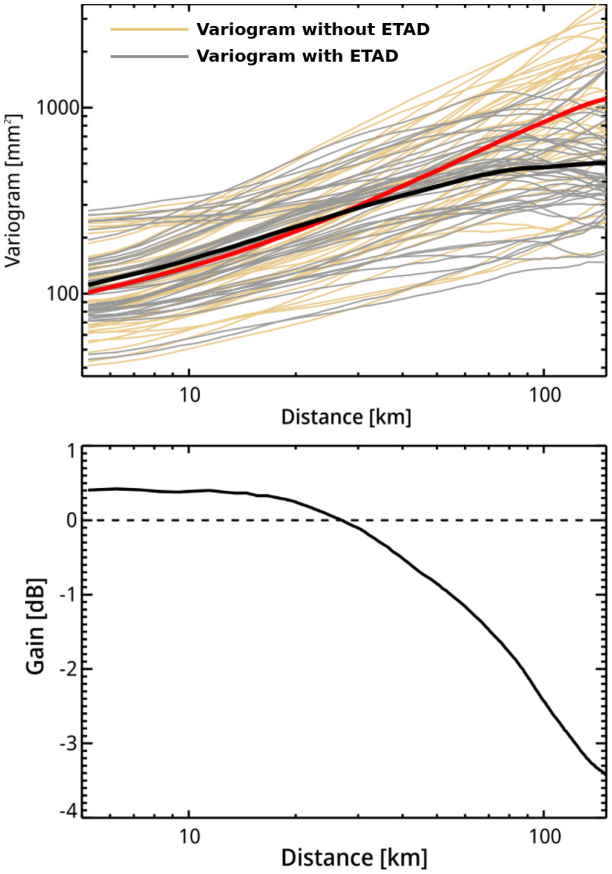

Fig. 10. (Top) Variograms of interferometric phase before and after ETAD-based correction for the 66 interferograms of the Norway test site. The thick red and black lines show the average variogram before and after correction, respectively. (Bottom) Ratio of variograms before Γ and after Γ_{etad} correction, in dB as function of distance, gain $= 10\log_{10}(\Gamma_{\text{etad}}/\Gamma)$.

E. Stratification Considerations

The stratification influences the variogram at a broad range of spatial scales, and any potential improvement should theoretically be quantifiable. For this particular study, stratification is not significantly affecting more than a small percentage of the total area of interest, leading to a smear effect that makes it hard to quantify the effect of ETAD-based stratification correction in isolation. Thus, an overall variogram analysis of the whole area is not a suitable method for a direct quantitative analysis of stratification correction.

Nevertheless, some insight in the effect of ETAD corrections can be obtained by reducing the analyzed area to valleys where the stratification effect is dominant. The analyzed area is marked in Fig. 9. We inverted the stack of unwrapped interferograms of the reduced area with respect to a temporal reference and a high-coherence reference point (i.e., straightforward short baseline subset-like inversion, see, e.g., [72]). The result is a single-reference stack of 11 differential interferograms, each representing the phase difference between the first scene and each of the other scenes. By assuming that no significant motion happened during the 66-day time series and ignoring other noise terms, we may interpret these interferograms as APS only.

By comparing the inverted stack before and after ETAD correction, the effect on the stratification can be visually inspected. Fig. 12 shows two examples. The first example is the typical case, where no residual stratification can be identified by visual inspection after correction. The second example is the only example in this stack where the correction was suboptimal, and a barely visible residual stratification component is still present in the upper part of the corrected interferogram.

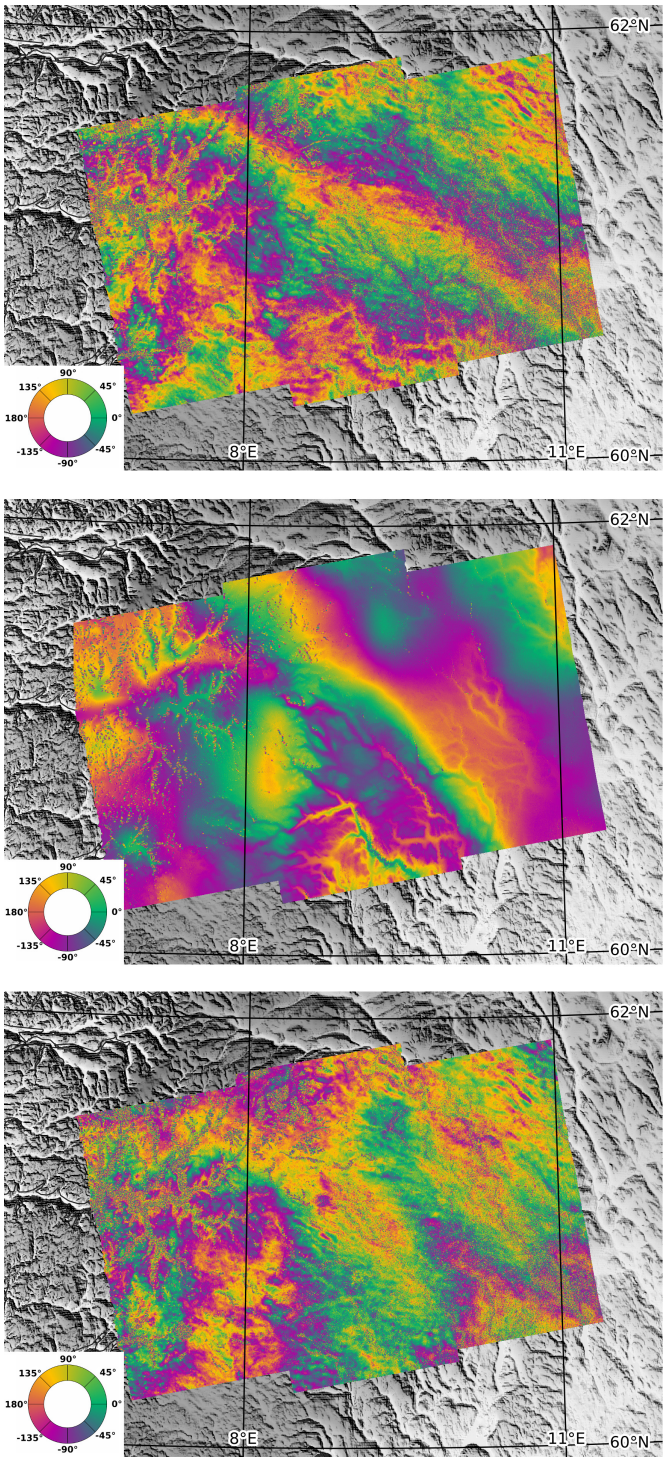

Fig. 11. Example illustrating the effect of ETAD correction, particularly the long wavelength component and stratification. (Top) Original interferogram. (Middle) ETAD correction. (Bottom) Corrected interferogram. One color cycle corresponds to half a wavelength change in slant range, about 28 mm.

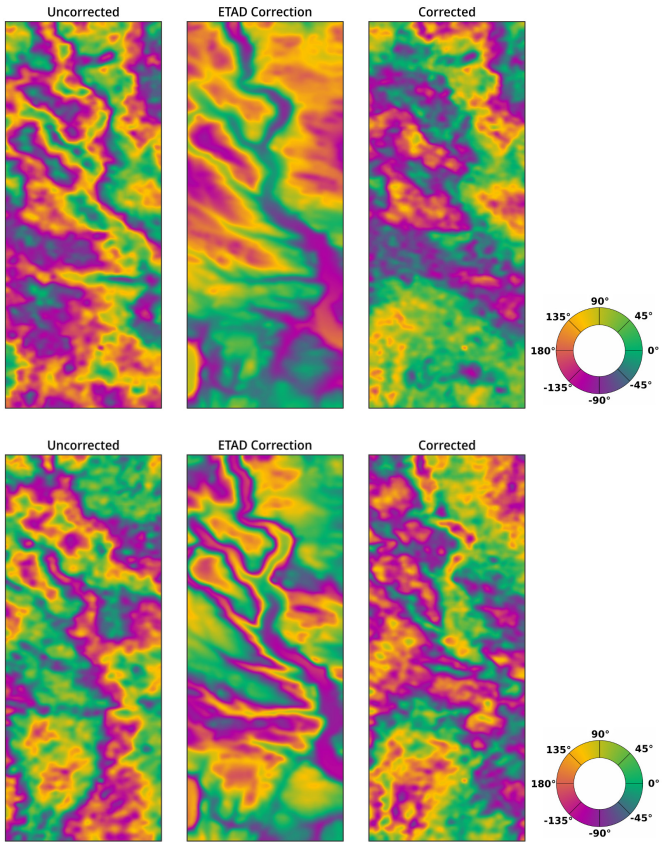

Fig. 12. (Top) Interferogram July 2, 2019, vs. August 7, 2019; illustrative (typical) example, stratification successfully mitigated. (Bottom) Interferogram July 2, 2019, vs. July 26, 2019—the only example of slightly suboptimal ETAD correction in the stack. One color cycle corresponds to half a wavelength change in slant range, about 28 mm. Results display subset as marked in Fig. 9.

VI. Conclusion and Outlook

In this article, we outlined the ETAD product for S-1 SLC SAR images, presented the validation at geodetic calibration sites, and evaluated first applications to assess and demonstrate product usability. Product structure, the underlying algorithms, and its usage were discussed and examples are shown to emphasize the need for such timing corrections in SAR applications. The product comprises the corrections for tropospheric delay, ionospheric delay, solid Earth tides displacement, and the SAR processor effects of bistatic azimuth shifts, Doppler shifts in range, and azimuth shifts due to azimuth FM rate mismatch, which in total can amount to several meters in range and azimuth, respectively.

The product was verified in dedicated geolocation experiments with accurately surveyed CRs and evaluated in two well-established SAR applications: ice velocity monitoring with OT and ground motion mapping with interferometry. The geolocation assessment performed at test sites in Australia, Finland, and Germany confirms that the ETAD corrections meet the formal 1 sigma specification of ± 0.20 m in range and ± 0.10 m in azimuth. In general, we obtained experimental ALE results of better than 0.05 m. The result of 0.33 m obtained for the IW azimuth data is a consequence of the SAR image resolution and not of the ETAD product. Moreover, a bias of 0.15 m was found in the azimuth geolocation results of SM data and has to be addressed by an update of S-1A and S-1B sensor timing calibration used in ETAD. From these results, we conclude that the high geolocation accuracy, which is attainable with S-1 data [23], [36], is now operationally accessible at a global scale.

For OT IV monitoring, ETAD products constitute an opportunity to get free from the need of stable calibration areas for bias correction, which are not always available in the acquired scenes. In the Greenland study case, two approaches have been tested for correcting biases with ETAD products: the *a priori* timing correction of SLCs, and the postprocessing correction of OT results. Both the methods are easily integrated as optional modules in standard processing chains. It has been demonstrated with practical examples that both the approaches yield similar performances. With both the methods, long-scale trends are removed and the residual velocity biases are reduced down to subcentimetric values, which is about the limit of the performance expected for offset-tracking. The improvement is particularly significant for 6-day pairs that are more affected by timing delays than 12-day pairs. For operational IV monitoring, our recommendation goes toward the postprocessing corrections, which involve less computational cost and less storage memory, and enable the reprocessing of archive results.

In the Norway case study, we have tested the performance of ETAD corrections for InSAR time series applications. A variogram analysis of all the interferograms before and after ETAD correction showed that atmospheric phase components of spatial scales larger than 25 km are effectively mitigated. A visual inspection of the interferograms before and after correction indicates that also the atmospheric stratification is mitigated very well by ETAD in almost all the cases. Although the analysis presented here shows a clear potential for operational utilization of ETAD, it should be noted that due to the presence of significant (unpredictable) turbulent atmosphere in this particular area, more data from multiple summer seasons are needed to quantitatively evaluate the performance effect for the stratification component. Moreover, the ionospheric layer provided with the ETAD product is targeting large-scale pixel localization errors, whereas for interferometry the split-spectrum methods as described in [75] could be combined with ETAD to compensate for high-frequency ionospheric variations. Further verification and refinement of the presented approach with more data and at other locations worldwide would comprise a logical subject for future work.

At the time of writing (autumn 2021), activities for the integration of the SETAP software into the S-1 ground segment are ongoing. According to the current plans, preoperations (not open to user) are set to start by the last quarter of 2021. Sustaining the ETAD production as part of S-1 routine operations, i.e., routine generation of the product in line with the SAR image products, will then be contemplated on the basis of an assessment of the preoperational production. In addition, ESA is currently supporting the hosting of SETAP in the Geohazards Exploitation Platform (GEP) to promote the early usage of the ETAD product from expert users of different

application domains and gather valuable feedback from the community [76]. After the product is brought into operations, and assuming a positive response from the community, ESA will evaluate possible alternatives to make ETAD products available also for historical S-1A and S-1B data.

Future maintenance of the processor and ETAD product quality is foreseen by the S-1 mission performance cluster that is responsible for calibration, validation, quality control, and end-to-end system performance assessment of all S-1 products [36]. This will also involve the maintenance of the SETAP auxiliary data files such as the timing calibration, which has to be refined for the SM azimuth data. Once the product has become fully integrated into regular operations, the accuracy gain using ETAD data can greatly simplify the processing steps in SAR applications, e.g., by making tie-points obsolete, and it will significantly improve the quality of displacement estimation with OT and InSAR methods.

ACKNOWLEDGMENT

The authors would like to thank all the colleagues from DLR and ESA who contributed to this project, as well as ENVEO and PPO.labs for feedback and performing first pilot studies with ETAD products. Finally, the authors thank the anonymous reviewers who provided valuable comments to improve the article. The views expressed herein can in no way be taken to reflect the official opinion of the European Space Agency or the European Union.

REFERENCES

[1] J. Curlander and R. McDonough, *Synthetic Aperture Radar: Systems and Signal Processing*. Hoboken, NJ, USA: Wiley, 1991.

[2] I. G. Cumming and F. H. Wong, *Digital Processing of Synthetic Aperture Radar Data*. Norwood, MA, USA: Artech House, 2005.

[3] M. Eineder, "Ocillator clock drift compensation in bistatic interferometric SAR," in *Proc. IGARSS*, Toulouse, France, Jul. 2003, pp. 1449–1451.

[4] G. Krieger and M. Younis, "Impact of oscillator noise in bistatic and multistatic SAR," *IEEE Geosci. Remote Sens. Lett.*, vol. 3, no. 3, pp. 424–428, Jul. 2006.

[5] T. Hobiger, R. Ichikawa, Y. Koyama, and T. Kondo, "Fast and accurate ray-tracing algorithms for real-time space geodetic applications using numerical weather models," *J. Geophys. Res.*, vol. 113, pp. 1–14, Oct. 2008.

[6] G. Möller, R. Weber, and J. Böhm, "Improved troposphere blind models based on numerical weather data," *Navigation*, vol. 61, no. 3, pp. 203–211, Sep. 2014.

[7] X. Cong, U. Balss, F. Rodriguez Gonzalez, and M. Eineder, "Mitigation of tropospheric delay in SAR and InSAR using NWP data: Its validation and application examples," *Remote Sens.*, vol. 10, no. 10, pp. 1–21, 2018.

[8] C. Yu, Z. Li, and G. Blewitt, "Global comparisons of ERA5 and the operational HRES tropospheric delay and water vapor products with GPS and MODIS," *Earth Space Sci.*, vol. 8, no. 5, pp. 1–18, May 2021.

[9] M. Hernández-Pajares *et al.*, "The IGS VTEC maps: A reliable source of ionospheric information since 1998," *J. Geod.*, vol. 83, nos. 3–4, p. 263, 2009.

[10] M. Hernández-Pajares *et al.*, "The ionosphere: Effects, GPS modeling and the benefits for space geodetic techniques," *J. Geodesy*, vol. 85, no. 12, pp. 887–907, 2011.

[11] J. Böhm and H. Schuh, Eds., *Atmospheric Effects in Space Geodesy*. Berlin, Germany: Springer-Verlag, 2013.

[12] F. Massmann, K. Neumayer, J. Raimondo, K. Enninghorst, and H. Li, "Quality of the D-PAF ERS orbits before and after the inclusion of PRARE data," in *Proc. 3rd ERS Symp.*, Florence, Italy, 1997, pp. 1655–1660.

[13] H. Peter *et al.*, "Sentinel-1A—First precise orbit determination results," *Adv. Space Res.*, vol. 60, no. 5, pp. 879–892, Sep. 2017.

[14] O. Montenbruck, S. Hackel, and A. Jäggi, "Precise orbit determination of the Sentinel-3A altimetry satellite using ambiguity-fixed GPS carrier phase observations," *J. Geodesy*, vol. 92, no. 7, pp. 711–726, Jul. 2018.

[15] S. Hackel, C. Gisinger, U. Balss, M. Wermuth, and O. Montenbruck, "Long-term validation of TerraSAR-X and TanDEM-X orbit solutions with laser and radar measurements," *Remote Sens.*, vol. 10, no. 5, pp. 1–20, 2018.

[16] D. Arnold, O. Montenbruck, S. Hackel, and K. Sośnica, "Satellite laser ranging to low Earth orbiters: Orbit and network validation," *J. Geodesy*, vol. 93, no. 11, pp. 2315–2334, Nov. 2019.

[17] P. Teunissen and O. Montenbruck, Eds., *Springer Handbook of Global Navigation Satellite Systems*. Cham, Switzerland: Springer, 2017.

[18] M. Eineder, C. Minet, P. Steigenberger, X. Cong, and T. Fritz, "Imaging geodesy—Toward centimeter-level ranging accuracy with TerraSAR-X," *IEEE Trans. Geosci. Remote Sens.*, vol. 49, no. 2, pp. 661–671, Feb. 2011.

[19] X. Cong, U. Balss, M. Eineder, and T. Fritz, "Imaging geodesy—Centimeter-level ranging accuracy with TerraSAR-X: An update," *IEEE Geosci. Remote Sens. Lett.*, vol. 9, no. 5, pp. 948–952, Sep. 2012.

[20] C. Gisinger *et al.*, "Precise three-dimensional stereo localization of corner reflectors and persistent scatterers with TerraSAR-X," *IEEE Trans. Geosci. Remote Sens.*, vol. 53, no. 4, pp. 1782–1802, Apr. 2015.

[21] U. Balss, C. Gisinger, and M. Eineder, "Measurements on the absolute 2-D and 3-D localization accuracy of TerraSAR-X," *Remote Sens.*, vol. 10, no. 656, pp. 1–21, 2018.

[22] U. Balss, C. Gisinger, M. Eineder, H. Breit, A. Schubert, and D. Small, *Survey Protocol for Geometric SAR Sensor Analysis*, document DLR-FRM4SAR-TN-200, Issue 1.4, Apr. 2018. Accessed: Jul. 4, 2022. [Online]. Available: http://calvalportal.ceos.org/calibration-methods-guidelines

[23] C. Gisinger *et al.*, "In-depth verification of Sentinel-1 and TerraSAR-X geolocation accuracy using the Australian corner reflector array," *IEEE Trans. Geosci. Remote Sens.*, vol. 59, no. 2, pp. 1154–1181, Feb. 2021.

[24] A. L. Gray, N. Short, K. E. Mattar, and K. C. Jezek, "Velocities and flux of the Filchner ice shelf and its tributaries determined from speckle tracking interferometry," *Can. J. Remote Sens.*, vol. 27, no. 3, pp. 193–206, Jun. 2001.

[25] I. Joughin, "Ice-sheet velocity mapping: A combined interferometric and speckle-tracking approach," *Ann. Glaciol.*, vol. 34, no. 1, pp. 195–201, 2002.

[26] T. Strozzi, A. Luckman, T. Murray, U. Wegmüller, and C. Werner, "Glacier motion estimation using SAR offset-tracking procedures," *IEEE Trans. Geosci. Remote Sens.*, vol. 40, no. 11, p. 2384—2391, Nov. 2002.

[27] T. Nagler, H. Rott, M. Hetzenecker, J. Wuite, and P. Potin, "The Sentinel-1 mission: New opportunities for ice sheet observations," *Remote Sens.*, vol. 7, no. 7, pp. 9371–9389, 2015.

[28] C. Meertens, B. Brooks, J. Foster, and M. Miller. *Troposphere, Ionosphere, GPS, and Interferometric Radar (TIGIR) Workshop Proposal, Proposal Submitted to NSF EAR Geophysics*. Accessed: Jul. 4, 2022. [Online]. Available: https://www.unavco.org

[29] B. Rommen *et al.*, "The ESA METAWAVE project: Correcting for atmospheric water vapour effects in InSAR products," in *3rd Eur. Conf. Antennas Propag.*, 2009, pp. 3428–3432.

[30] E. Hólm, R. Forbes, S. Lang, L. Magnusson, and S. Malardel, "New model cycle brings higher resolution," ECMWF Newslett., ECMWF, Reading, U.K., ECMWF Newslett. 147, 2016, pp. 14–19. Accessed: Jul. 4, 2022. [Online]. Available: http://www.ecmwf.int/sites/default/files/elibrary/2016/16299-newsletter-no147-spring-2016.pdf

[31] M. Bourbigot, H. Johnsen, and R. Piantanida, *Sentinel-1 Product Definition*, document S1-RS-MDA-52-7440, Issue 2, Revision 7, Sentinel-1 Mission Performance Center (MPC), Mar. 2016. Accessed: Jul. 4, 2022. [Online]. Available: https://sentinel.esa.int/web/sentinel/user-guides/document-library

[32] J. C. Curlander, "Location of spaceborne SAR imagery," *IEEE Trans. Geosci. Remote Sens.*, vol. GE-20, no. 3, pp. 359–364, Jul. 1982.

[33] T. Fritz, L. Krieger, C. Gisinger, and M. Lachaise, *S1-ETAD Project Product Definition Document*, ESA Tech. document ETAD-DLR-PS-0002, Issue 2.1, Jun. 2021. Accessed: Jul. 4, 2022. [Online]. Available: https://sentinel.esa.int/web/sentinel/missions/sentinel-1/data-products/etad-dataset

[34] L. Krieger, T. Fritz, C. Gisinger, and M. Lachaise, *S1-ETAD Project Product Format Specification*, ESA Tech. document ETAD-DLR-PS-0014, Issue 1.5, Jun. 2021. Accessed: Jul. 4, 2022. [Online]. Available: https://sentinel.esa.int/web/sentinel/missions/sentinel-1/data-products/etad-dataset

[35] S. Mbaye and M. Moucha, *Standard Archive Format for Europe SAFE Control Book Volume 1 Core Specification*, ESA Tech. document PGSI-GSEG-EOPG-FS-05-0001, Issue 1.0, Aug. 2005.

[36] G. Hajduch *et al.*, *S-1A & S-1B Annual Performance Report 2020*, ESA Tech. document MPC-0504, Issue 1.1, Mar. 2021. Accessed: Jul. 4, 2022. [Online]. Available: https://sentinel.esa.int/documents/247904/3406423/Sentinel-1-Annual-Performance-Report-2018.pdf

[37] E. Fahrland, P. Jacob, H. Schrader, and H. Kahabka, *Copernicus Digital Elevation Model Product Handbook*, Copernicus Tech. document GEO.2018-1988-2, Issue 3.0, Nov. 2020. Accessed: Jul. 4, 2022. [Online]. Available: https://spacedata.copernicus.eu

[38] N. K. Pavlis, S. A. Holmes, S. C. Kenyon, and J. K. Factor, "The development and evaluation of the Earth gravitational model 2008 (EGM2008)," *J. Geophys. Res.*, vol. 117, Apr. 2012, Art. no. B04406.

[39] *World Geodetic System 1984—Its Definition and Relationships With Local Geodetic Systems*, NIMA Tech. document TR8350.2, Issue 3.1, National Imagery and Mapping Agency, Jan. 2000.

[40] C. Gisinger, U. Balss, S. Suchandt, and T. Fritz, *S1-ETAD Project Algorithm Technical Baseline Document*, ESA Tech. document ETAD-DLR-DD-0008, Issue 2.1, Apr. 2020. Accessed: Jul. 4, 2022. [Online]. Available: https://sentinel.esa.int/web/sentinel/missions/sentinel-1/data-products/etad-dataset

[41] A. Hofmeister, "Determination of path delays in the atmosphere for geodetic VLBI by means of ray-tracing," Ph.D. thesis, Dept. Geodesy Geoinf., Tech. Univ. Vienna, Vienna, Austria, 2016. Accessed: Jul. 4, 2022. [Online]. Available: http://katalog.ub.tuwien.ac.at/AC13248753

[42] ECMWF. (2021). *IFS Documentation CY47R3*. Accessed: Jul. 4, 2022. [Online]. Available: https://www.ecmwf.int/en/publications/ifs-documentation

[43] J. Wallace and P. Hobbs, *Atmospheric Science: An Introductory Survey*, 2nd ed. Amsterdam, The Netherlands: Elsevier, 2006.

[44] E. K. Smith and S. Weintraub, "The constants in the equation for atmospheric refractive index at radio frequencies," *Proc. Inst. Radio Eng.*, vol. 41, no. 8, pp. 1035–1037, Aug. 1953.

[45] A. Villiger and R. Dach, Eds., *International GNSS Service Technical Report 2020*. Bern, Switzerland: Univ. of Bern, 2021. Accessed: Jul. 4, 2022. [Online]. Available: https://www.igs.org

[46] S. Schaer, *Mapping and Predicting the Earth's Ionosphere Using the Global Positioning System* (Geodaetisch-geophysikalische Arbeiten in der Schweiz), vol. 59. Zürich, Switzerland: Schweizerische Geodaetische Kommission, 1999. Accessed: Jul. 4, 2022. [Online]. Available: http://www.sgc.ethz.ch/publications

[47] B. Hofmann-Wellenhof, H. Lichtenegger, and E. Wasle, *GNSS Global Navigation Satellite Systems*. New York, NY, USA: Springer, 2008.

[48] G. Petit and B. Luzum, Eds., *IERS Conventions (2010)*. Frankfurt, Germany: Verlag des Bundesamts für Kartographie und Geodäsie, 2010. Accessed: Jul. 4, 2022. [Online]. Available: http://tai.bipm.org/iers/conv2010/conv2010.html

[49] C. H. Acton, "Ancillary data services of NASA's navigation and ancillary information facility," *Planetary Space Sci.*, vol. 44, no. 1, pp. 65–70, Jan. 1996.

[50] M. Bourbigot, H. Johnsen, and R. Piantanida, *Sentinel-1 Product Specification*, document S1-RS-MDA-52-7441, Issue 3, Revision 6, Sentinel-1 Mission Performance Center (MPC), Jun. 2016. Accessed: Jul. 4, 2022. [Online]. Available: https://sentinel.esa.int/web/sentinel/user-guides/document-library

[51] ESA. *Reader API for Sentinel-1 Extended Timing Annotation Dataset, GitLab Repository S1-ETAD maintained by ESA*. Accessed: Jul. 4, 2022. [Online]. Available: https://gitlab.com/s1-etad/s1-etad

[52] N. Yague-Martinez *et al.*, "Interferometric processing of Sentinel-1 TOPS data," *IEEE Trans. Geosci. Remote Sens.*, vol. 54, no. 4, pp. 2220–2234, Apr. 2016.

[53] M. Thankappan, M. Garthwaite, C. Gisinger, A. Schubert, P. Meadows, and N. Miranda, "Improvements to the position coordinates for the Australian corner reflector array and new infrastructure to support SAR calibration and multi-technique validation at the Yarragadee fundamental geodetic station," in *Proc. CEOS WGCV Workshop*, Buenos Aires, Argentina, Dec. 2018, pp. 1–16. Accessed: Aug. 8, 2022. [Online]. Available: https://calvalportal.ceos.org/html/portal/sarc/documents/documents/2018/index.html

[54] D. Small, B. Rosich, A. Schubert, E. Meier, and D. Nüesch, "Geometric validation of low and high-resolution ASAR imagery," in *Proc. ENVISAT ERS Symp.* Salzburg, Austria, Sep. 2005, pp. 1–9. Accessed: Aug. 8, 2022. [Online]. Available: https://www.geo.uzh.ch/microsite/rsl-documents/research/SARlab/Publications/Category/conferences.html

[55] A. Schubert, N. Miranda, D. Geudtner, and D. Small, "Sentinel-1A/B combined product geolocation accuracy," *Remote Sens.*, vol. 9, no. 6, p. 607, Jun. 2017.

[56] U. Balss *et al.*, "High precision measurement on the absolute localization accuracy of TerraSAR-X," in *Proc. IGARSS*, Munich, Germany, Jul. 2012, pp. 1625–1628.

[57] Z. Altamimi, P. Rebischung, L. Métivier, and X. Collilieux, "ITRF2014: A new release of the International Terrestrial Reference Frame modeling nonlinear station motions," *J. Geophys. Res. Solid Earth*, vol. 121, no. 8, pp. 6109–6131, Aug. 2016.

[58] A. Schubert, D. Small, N. Miranda, D. Geudtner, and E. Meier, "Sentinel-1A product geolocation accuracy: Commissioning phase results," *Remote Sens.*, vol. 7, no. 7, pp. 9431–9449, 2015.

[59] R. Bamler and M. Eineder, "Accuracy of differential shift estimation by correlation and split-bandwidth interferometry for wideband and delta-k SAR systems," *IEEE Geosci. Remote Sens. Lett.*, vol. 2, no. 2, pp. 151–155, Apr. 2005.

[60] R. Czikhardt, H. van der Marel, F. J. van Leijen, and R. F. Hanssen, "Estimating signal-to-clutter ratio of InSAR corner reflectors from SAR time series," *IEEE Geosci. Remote Sens. Lett.*, vol. 19, pp. 1–5, 2022.

[61] *Greenland Ice Sheet Annual Gridded Velocity Data From 2017 to Present Derived From Satellite Observations, Climate Data Store Maintained by ECMWF*, Copernicus Climate Change Service, Eur. Centre Medium-Range Weather Forecasts, Reading, U.K. Accessed: Jul. 4, 2022, doi: 10.24381/cds.0b96b838.

[62] R. Michel, J. P. Avouac, and J. Taboury, "Measuring ground displacements from SAR amplitude images: Application to the Landers earthquake," *Geophys. Res. Lett.*, vol. 26, no. 7, pp. 875–878, Apr. 1999.

[63] Y. Fialko, M. Simons, and D. Agnew, "The complete (3-D) surface displacement field in the epicentral area of the 1999 M_W 7.1 Hector mine earthquake, California, from space geodetic observations," *Geophys. Res. Lett.*, vol. 28, no. 16, pp. 3063–3066, Aug. 2001.

[64] M. Tobita, M. Murakami, H. Nakagawa, H. Yarai, S. Fujiwara, and P. A. Rosen, "3-D surface deformation of the 2000 Usu eruption measured by matching of SAR images," *Geophys. Res. Lett.*, vol. 28, no. 22, pp. 4291–4294, Nov. 2001.

[65] A. L. Gray, K. E. Mattar, and G. Sofko, "Influence of ionospheric electron density fluctuations on satellite radar interferometry," *Geophys. Res. Lett.*, vol. 27, no. 10, pp. 1451–1454, 2000.

[66] F. Rocca, "Modeling interferogram stacks," *IEEE Trans. Geosci. Remote Sens.*, vol. 45, no. 10, pp. 3289–3299, Oct. 2007.

[67] P. S. Agram and M. Simons, "A noise model for InSAR time series," *J. Geophys. Res., Solid Earth*, vol. 120, no. 4, pp. 2752–2771, 2015.

[68] R. Hanssen, *Radar Interferometry: Data Interpretation and Error Analysis*. Boston, MA, USA: Kluwer, 2001.

[69] N. Adam, "Methodology of a troposphere effect mitigation processor for SAR interferometry," *IEEE J. Sel. Topics Appl. Earth Observ. Remote Sens.*, vol. 12, no. 12, pp. 5334–5344, Dec. 2019.

[70] T. R. Lauknes, "InSAR tropospheric stratification delays: Correction using a small baseline approach," *IEEE Geosci. Remote Sens. Lett.*, vol. 8, no. 6, pp. 1070–1074, Nov. 2011.

[71] A. Ferretti, C. Prati, and F. Rocca, "Permanent scatterers in SAR interferometry," *IEEE Trans. Geosci. Remote Sens.*, vol. 39, no. 1, pp. 8–20, Jan. 2001.

[72] P. Berardino, G. Fornaro, R. Lanari, and E. Sansosti, "A new algorithm for surface deformation monitoring based on small baseline differential SAR interferograms," *IEEE Trans. Geosci. Remote Sens.*, vol. 40, no. 11, pp. 2375–2383, Nov. 2002.

[73] T. R. Emardson, M. Simons, and F. H. Webb, "Neutral atmospheric delay in interferometric synthetic aperture radar applications: Statistical description and mitigation," *J. Geophys. Res., Solid Earth*, vol. 108, no. B5, pp. 1–8, May 2003.

[74] A. Parizzi, R. Brcic, and F. De Zan, "InSAR performance for large-scale deformation measurement," *IEEE Trans. Geosci. Remote Sens.*, vol. 59, no. 10, pp. 8510–8520, Oct. 2021.

[75] G. Gomba, A. Parizzi, F. De Zan, M. Eineder, and R. Bamler, "Toward operational compensation of ionospheric effects in SAR interferograms: The split-spectrum method," *IEEE Trans. Geosci. Remote Sens.*, vol. 54, no. 3, pp. 1446–1461, Mar. 2016.

[76] J. M. B. Delgado. (2021). *Extending the Sentinel-1 Timing Annotation Datasets Using the ESA S1-ETAD Service, Service Note on ETAD Early Access in GEP Platform*. Accessed: Jul. 4, 2022. [Online]. Available: https://discuss.terradue.com/

Christoph Gisinger received the Diploma degree in geodesy from Technische Universität Graz, Graz, Austria, in 2010, and the M.Sc. degree in earth oriented space science and technologies and the Ph.D. degree in geodesy from Technische Universität München, Munich, Germany, in 2012 and 2019, respectively.

Since 2017, he has been with the Remote Sensing Technology Institute, German Aerospace Center (DLR), Weßling, Germany, where he is involved in the geodetic SAR processing of the missions TerraSAR-X and Sentinel-1. His research interests include positioning with SAR, correction modeling for absolute SAR observations, and radargrammetric image processing with a focus on fusing SAR with geodetic observations for new applications.

Ludivine Libert received the master's degree in space sciences and the Ph.D. degree in remote sensing from the Université de Liège, Liège, Belgium, in 2014 and 2018, respectively.

During her Ph.D., she spent four years with the Centre Spatial de Liège, Liège, Belgium, and studied SAR and SAR interferometry, with a focus on multispectral and multitemporal InSAR techniques for deformation monitoring. In 2019, she became a Research Scientist with ENVEO, Innsbruck, Austria, where her work focused on SAR and InSAR methods for ice and snow monitoring.

Petar Marinkovic received the M.Sc. degree in geodesy from the University of Belgrade, Belgrade, Serbia, in 1999, and the Ph.D. degree in physical geodesy and satellite radar interferometry from the University of Stuttgart, Stuttgart, Germany, and Technical University of Delft, Delft, The Netherlands, in 2008.

Early 2009, he founded PPO.labs, The Hague, The Netherlands, and has been leading it since. PPO.labs is a Research and Development consultancy company focusing on algorithmic and operational development for ground motion estimation using SAR interferometry.

Lukas Krieger received the B.Sc. degree in computer science from the Technische Universität München, Munich, Germany, in 2011, the M.Sc. degree in health informatics from the Karolinska Institutet, Stockholm, Sweden, in 2013, and the Ph.D. degree from the Faculty of Aerospace and Geodesy, Technische Universität München, in 2020.

In 2015, he joined the Remote Sensing Technology Institute, German Aerospace Center (DLR), Weßling, Germany. His research interests include correction modeling for absolute SAR observations, geodetic mass balance calculations for glaciers and ice sheets, and detection of the glacier grounding line with InSAR using the missions TerraSAR-X, TanDEM-X, and Sentinel-1.

Yngvar Larsen (Member, IEEE) received the M.Sc. degree in applied physics and the Ph.D. degree in physics from the University of Tromsø, Tromso, Norway, in 1999 and 2003, respectively.

Since 2007, he has been with NORCE (formerly Norut), Tromsø, Norway, as a Senior Researcher in the Earth Observation Group. His research interests include fundamental signal processing for SAR and interferometric SAR, including in particular focusing algorithms for new SAR missions and ground motion estimation using SAR interferometry.

Antonio Valentino received the master's degree in electronic engineering from the Politecnico di Torino, Torino, Italy, in 2000.

Since 2001, he has been working on synthetic aperture radar (SAR) processing, calibration, and applications. He worked on important international SAR missions, including COSMO-SkyMed, Sentinel-1, SAOCOM, and BIOMASS. He is currently a Contractor with the European Space Research Institute (ESRIN), European Space Agency (ESA), Frascati, Italy. He is Sentinel-1 SAR engineer working on calibration and SAR data quality.

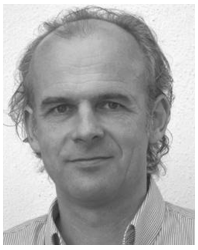

Helko Breit received the Diploma degree in electrical and telecommunication science from the Technical University of Munich, Munich, Germany, in 1990.

Since 1990, he has been with the German Aerospace Center (DLR), Weßling, Germany, where he is currently supervising the Synthetic Aperture Radar (SAR) Processor Development Team, Remote Sensing Technology Institute. He has worked on a variety of international missions, including SIR-C/X-SAR, SRTM/X-SAR, and the German missions TerraSAR-X/TanDEM-X. He contributed to several European Space Agency studies and supported the commissioning of the ESA's Sentinel 1 SAR satellites. He was responsible for the development of the TerraSAR-X multimode SAR processor TMSP and the bistatic processing of TanDEM-X mission data. His research activities comprise the development of SAR processing algorithms and systems for future SAR satellites and missions.

Ulrich Balss received the Diploma degree in physics and the Dr.phil.nat. degree from the Johann Wolfgang Goethe University, Frankfurt, Germany, in 1994 and 2004, respectively.

Between 2003 and 2010, he was the Scientific Staff with the Technical University Munich, Munich, Germany. In this time, he worked within the framework of a cooperation of the Technical University Munich and the German Aerospace Center (DLR), Weßling, Germany, and he was permanently located at the Remote Sensing Technology Institute (IMF) of the DLR. In 2010, he joined DLR's Remote Sensing Technology Institute. He is involved in the German TerraSAR-X and TanDEM-X missions. In particular, he participated in the development of the TerraSAR-X Multimode SAR Processor (TMSP) and implemented the focusing kernel of the TMSP.

Steffen Suchandt received the Dipl.-Ing. degree in electrical engineering from the University of Rostock, Rostock, Germany, in 1995.

From 1996 to 1998, he was with the Hochschule Wismar, Wismar, Germany, working on audiometry and otoacoustic emissions. Since 1998, he has been with the Remote Sensing Technology Institute of the German Aerospace Center (DLR), Weßling, Germany, working on numerous aspects of synthetic aperture radar (SAR). He was engaged in processor development and data calibration for the Shuttle Radar Topography Mission SRTM/X-SAR, was responsible for the development of a traffic data extraction system for the TerraSAR-X mission, and he was a system engineer in design and development of the SAR geodesy processor SAR Geodesy Processor (SGP) and the Sentinel-1 extended timing annotation data processor SETAP. He has wide experience in SAR interferometry, and signal and image processing and in software design. His research is focused on multichannel space borne SAR oceanography and on SAR geodesy.

Thomas Nagler (Member, IEEE) received the M.Sc. degree in meteorology and the Ph.D. degree in natural sciences from the University of Innsbruck, Innsbruck, Austria, in 1991 and 1996, respectively.

From 1991 to 2004, he was a Research Scientist with the Institute of Meteorology and Geophysics, University of Innsbruck. He is a Cofounder and, since 2001, the Managing Director of Environmental Earth Observation Information Technology (ENVEO IT) GmbH, Innsbruck. He has been a Principle/Coinvestigator and the Coordinator for several projects of ESA, the European Commission, and the Austrian Research Promotion Agency. He is/was a member of the Mission Advisory Group for Copernicus ROSE-L and Sentinel-1-NG. He has participated in several scientific expeditions to Patagonia, Antarctica, and Alpine Glaciers, and was leading/participating in international field campaigns in preparation for new satellite systems. His main research interests include retrieval methods and applications of microwave and optical remote sensing for snow hydrology, climatology, monitoring Alpine and polar glaciers and ice sheets, and assimilation of remote sensing products into geophysical process models.

Michael Eineder (Fellow, IEEE) received the Diploma degree in electrical engineering from Technische Universität München (TUM), Munich, Germany, in 1990, and the Dr.rer.nat. degree from the University of Innsbruck, Innsbruck, Austria, in 2004.

Since 2013, he has been an honorary Professor with TUM, where he is also currently a part-time Lecturer of remote sensing. He is also currently the Head of the SAR Signal Processing Department, Remote Sensing Technology Institute, German Aerospace Center (DLR), Weßling, Germany. His responsibilities encompass the development of SAR and interferometric SAR processing systems for current and future radar missions. Since 1990, he has been with DLR, where he has worked on a variety of international missions, including SIR-C/X-SAR, SRTM/X-SAR in cooperation with the National Aeronautics and Space Administration, ERS-1 (European Space Agency), and TerraSAR-X and TanDEM-X (Germany). His research interest is focused on future SAR missions and on imaging geodesy, an absolute positioning technique exploiting high-resolution SAR.

Nuno Miranda received the master's degree in telecommunications engineering from the University of Bordeaux, Talence, France, in 1999.

Since 2000, he has been working on synthetic aperture radar (SAR) application (interferometry) and calibration. He is currently with the European Space Research Institute (ESRIN), European Space Agency (ESA), Frascati, Italy. He is responsible for algorithm and processor development and calibration for the ESA SAR missions (ERS, ASAR, and Sentinel-1).